



Evaluating the 2020 European Seismic Hazard Model (ESHM20) using ShakeMap-derived ground motion fields in Greece

Nikolaos Anterriotis-Kalpakidis¹ · Anastasia Kiratzi¹

Received: 8 April 2025 / Accepted: 10 March 2026
© The Author(s) 2026

Abstract

This study evaluates the consistency between the 2020 European Seismic Hazard Model (ESHM20) and ShakeMap-derived ground-motion fields in Greece. A total of 2,617 ShakeMaps covering the period 1973–2022 were generated using regionally appropriate ground-motion models and adjusted to rock-site conditions following ESHM20 conventions (RotD50). Observational constraints in the form of strong-motion recordings and/or macroseismic intensities were available for 441 earthquakes, providing direct anchoring for a substantial subset of events, while the remaining fields rely primarily on model-based spatial interpolation. Exceedance fractions for peak ground acceleration (PGA) and 5% damped spectral acceleration at periods of 0.3 s and 1.0 s were evaluated relative to ESHM20 hazard maps for return periods of 50 and 475 years and across multiple aggregation levels (mean; 16th, 50th, and 84th percentiles). The resulting exceedance patterns exhibit the expected ordering across aggregation levels and broadly align with probabilistic seismic hazard expectations. Residual differences are more pronounced for spectral accelerations and in regions near site-classification thresholds, reflecting the combined influence of ground-motion model variability, site-response representation, and ShakeMap uncertainty. Given the limited 50-year observation window and the spatial correlation of earthquake ground motion, the results are interpreted as quantitative indicators of model consistency within epistemic uncertainty rather than as formal validation of the hazard model. The proposed framework provides a transparent and reproducible approach for national-scale screening of regional seismic hazard model behaviour.

Keywords Seismic hazard · PSHA · ShakeMaps · ESHM20 · Greece

✉ Nikolaos Anterriotis-Kalpakidis
nanterr@geo.auth.gr

Anastasia Kiratzi
kiratzi@geo.auth.gr

¹ Department of Geophysics, Aristotle University of Thessaloniki, Thessaloniki, Greece

1 Introduction

A fundamental objective in earthquake engineering is to ensure that buildings and infrastructure can withstand the anticipated levels of ground shaking during earthquakes. The expected shaking intensity at any site is a function of earthquake magnitude, source-to-site distance (including attenuation effects), and local site conditions. Probabilistic Seismic Hazard Assessment (PSHA) provides a systematic framework for quantifying and integrating these factors to describe the expected distribution of future ground shaking at a site. The primary output of PSHA is hazard maps, which are essential for assessing seismic hazard levels and informing design codes and standards in earthquake engineering.

Hazard maps typically assume rock-site conditions and specify a fixed probability of exceedance, p , over a defined time interval, Δt or, equivalently, a return period, RP. The probability, p , that a site experiences exceedance of a specific intensity measure (IM) threshold in the time interval, Δt , is given by:

$$p = 1 - e^{-\Delta t / RP} \quad (1)$$

if earthquake occurrence follows a Poisson process and that exceedance events are statistically independent. Under this assumption, the return period RP represents the average time interval between exceedances of a given intensity level at a site. Equation (1) therefore links the return period used in hazard maps to the probability that the corresponding intensity threshold will be exceeded at least once within a specified time window.

If N sites are considered and each site has an exceedance probability p over the time interval Δt , the expected number of sites experiencing exceedance is $N \times p$. This relationship allows exceedance probabilities defined in time to be interpreted in a spatial sense, a concept commonly referred to as “trading time for space”.

Previous studies (e.g., Cito et al. 2024) have applied this concept to assess the consistency of PSHA models against observed ground motions. For instance, comparisons between ShakeMap-derived IM values and PSHA hazard estimates over several return periods (50, 475, 975, and 2475 years) have generally demonstrated consistency for return periods up to 975 years, with discrepancies arising primarily for very long return periods due to the limited observational record. Other efforts have compared PSHA outputs with ground motion data obtained from instrumental recordings and macroseismic intensity observations (Albarelli and D’Amico 2008; Tasan et al. 2014; Manea et al. 2024; Rey et al. 2018). Nonetheless, direct validation of PSHA remains challenging because most instrumental or historical catalogues are relatively short compared to the timescales addressed by hazard models. To address these challenges, modern approaches integrate ShakeMaps, ground-motion prediction models (GMMs), and ground-motion intensity conversion equations (GMICEs) to increase the spatial sampling of shaking and support consistency-based model evaluation (Allen et al. 2009, 2023; Pothon et al. 2020).

In this study, we assess whether ShakeMap-derived intensity measures (IMs) for Greece over the period 1973–2022 are broadly compatible with the probabilistic bounds of the 2020 European Seismic Hazard Model (ESHM20) at the national scale. The ShakeMap fields analysed here are hybrid products: they incorporate strong-motion recordings and/or macroseismic intensity observations where available and rely on ground-motion models and spatial interpolation elsewhere. Observational constraints are available for 441 earthquakes,

meaning that many exceedance-generating events are observation-anchored; however, the resulting gridded shaking fields remain partly model-based. Consequently, and consistent with recent guidance on hazard-model evaluation (Marzocchi et al. 2025), the comparisons presented here are interpreted as national-scale consistency assessments within modelling uncertainty, rather than as strict validation tests against fully independent spatial observations of ground motion.

2 Overview of the tectonic setting and PSHA models for Greece

The Aegean region is characterized by a complex seismotectonic framework that includes subduction-related thrusting, large-scale strike-slip faulting, and widespread extensional normal faulting, collectively responsible for the high seismic hazard of Greece. The dominant tectonic feature is the Hellenic Subduction Zone, where the African lithosphere subducts beneath the Aegean microplate at rates of approximately 35–40 mm/yr (Reilinger et al. 2010). This process generates frequent intermediate-depth seismicity along the Wadati–Benioff zone and is associated with the development of the South Aegean Volcanic Arc, extending from the Saronic Gulf to the Dodecanese islands. Slab rollback along the Hellenic Subduction Zone drives back-arc extension, expressed as normal faulting across mainland Greece and the Aegean Sea (Le Pichon and Angelier 1979; Jolivet et al. 2013). To the north, the westward motion of the Anatolian plate, driven by collision with the Arabian plate, is accommodated by the North Anatolian Fault Zone (NAFZ), a major right-lateral strike-slip system that extends into the North Aegean Trough. This active tectonic corridor links Anatolia with the Aegean domain and has played a key role in regional stress accumulation and seismicity (Kiritzi 2002; Chousianitis et al. 2024 and references therein).

Figure 1 summarizes the principal tectonic structures together with population distribution. Nearly 47% of Greece’s population is concentrated in the metropolitan areas of Athens and Thessaloniki, both located in proximity to active fault systems. Historical earthquakes, including the Mw 5.9 Athens event of 7 September 1999 and the Mw 6.5 Thessaloniki event of 20 June 1978, illustrate the significant seismic risk affecting these urban centers.

Probabilistic seismic hazard assessments for Greece have been developed at various spatial scales (Papazachos et al. 1990; Tsapanos et al. 2009; Tselentis and Danciu 2010; Slejko et al. 2010, 2021; Stylianou et al. 2016; Vamvakaris et al. 2017; Vavlas et al. 2019; Kaviris et al. 2022; Sotiriadis et al. 2023). Greece is also represented in global and regional initiatives, including the Global Seismic Hazard Assessment Program (GSHAP; Giardini et al. 1999) and the European seismic hazard models ESHM13 (Woessner et al. 2015) and ESHM20 (Danciu et al. 2021).

ESHM20, which is the focus of this study, represents the most recent European-scale seismic hazard model for the Euro-Mediterranean region. It incorporates updated seismogenic source models, revised earthquake catalogues, detailed active-fault information, and a refined ground-motion model logic tree. Hazard estimates are provided for a wide range of spectral periods and return periods, from 50 to 5,000 years, supporting future revisions of Eurocode 8 provisions (CEN 2004). Figure 2 presents the spatial distribution of PGA hazard estimates for Greece derived from ESHM20, including mean values and the 16th, 50th (median), and 84th percentile levels for a 475-year return period. The strong spatial variability evident in these maps reflects the tectonic complexity of the Aegean region and

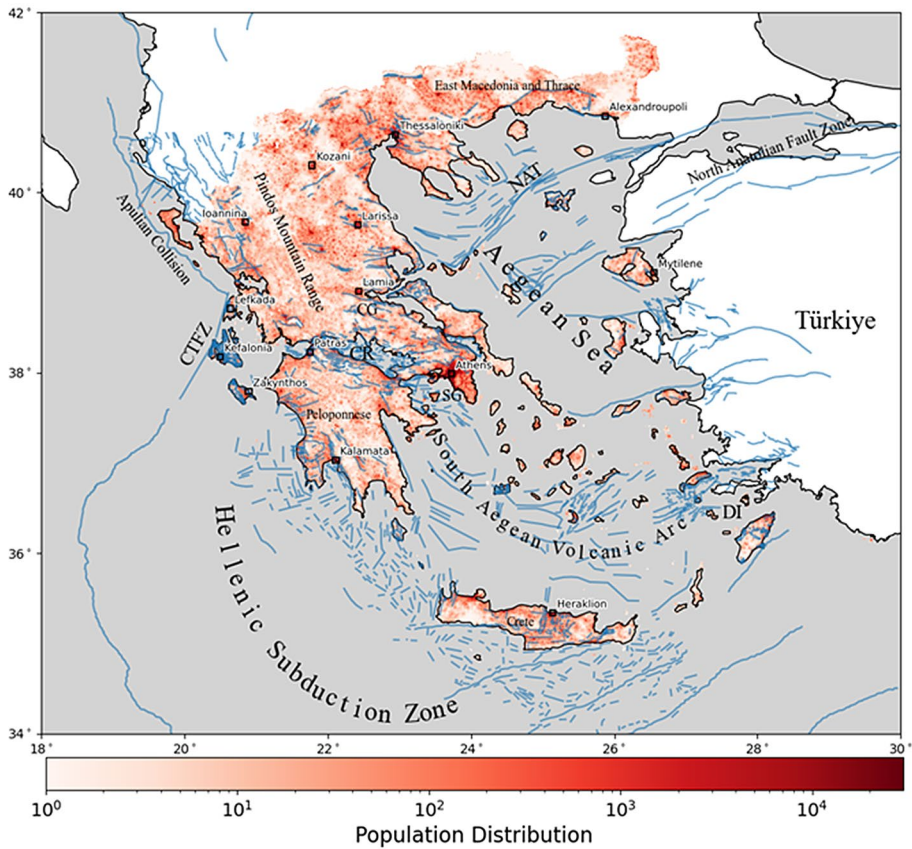


Fig. 1 Simplified seismotectonic setting of Greece showing the spatial distribution of major active faults (blue lines; NOFAULTSv.6; Ganas et al. 2013) together with population density, according to the colour scale. (source: Hellenic Statistical Authority). Key tectonic regions are indicated: NAT: North Aegean Trough, CR: Corinth Rift, CTFZ: Cephalonia Transform Fault Zone, CG: Central Greece, SG: Saronic Gulf, DI: Dodecanese Islands

provides the reference framework against which ShakeMap-derived exceedances are evaluated in this study.

3 Data and methods

The analysis follows a structured workflow including: (i) compilation and homogenization of an earthquake catalogue based on the USGS Comprehensive Catalogue (ComCat), to ensure internal magnitude consistency across the 50-year period through conversion of magnitudes to a unified potency magnitude scale; (ii) generation of ShakeMaps for all selected events using the USGS ShakeMap software; (iii) computation of peak ground acceleration (PGA) and spectral accelerations on a regular spatial grid; (iv) adjustment of the ShakeMap-derived intensity measures to rock-site conditions consistent with ESHM20 assumptions;

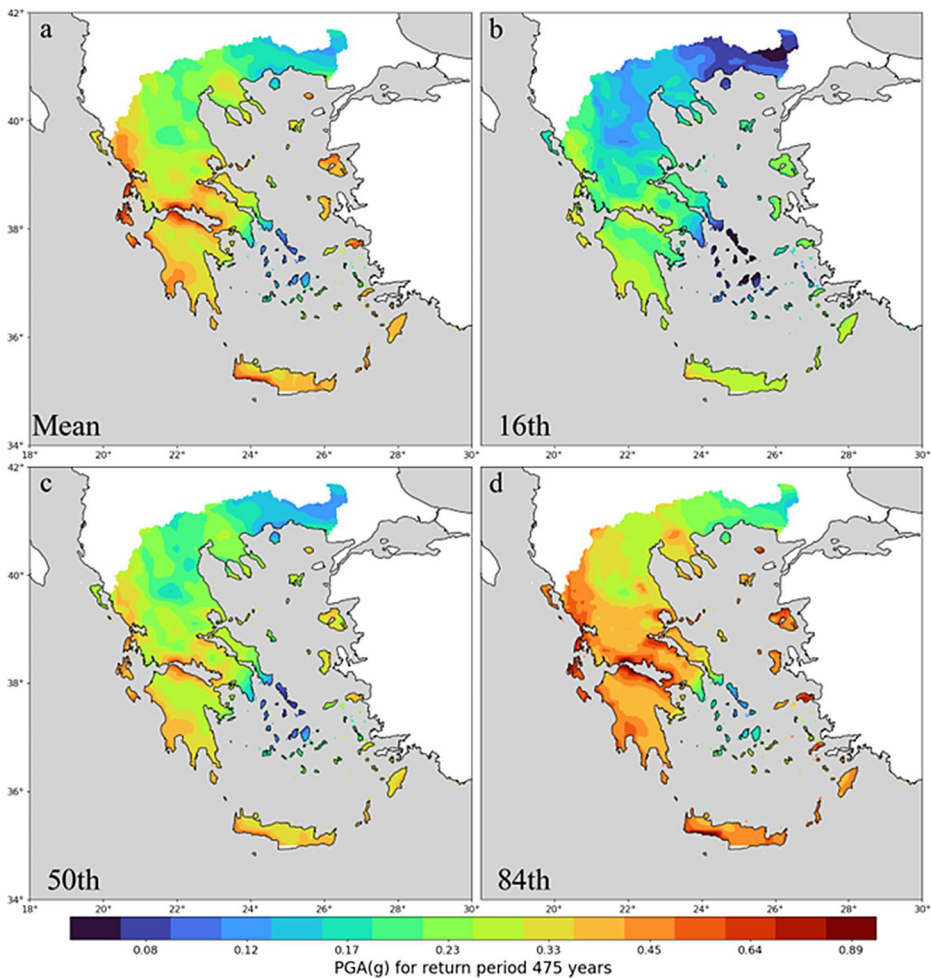


Fig. 2 Spatial distribution of peak ground acceleration (PGA) for Greece as predicted by the 2020 European Seismic Hazard Model (ESHM20; Danciu et al. 2021) for a return period of 475 years, corresponding to a 10% probability of exceedance in 50 years. Panels show different aggregation levels of the hazard model: (a) mean PGA, (b) 16th percentile, (c) 50th percentile (median), and (d) 84th percentile. PGA values are expressed in units of g

(v) comparison of the resulting intensity measures with ESHM20 hazard estimates at multiple aggregation levels and return periods; and (vi) statistical evaluation of exceedance areas using observed counts, theoretical binomial distributions, and the overlapping coefficient as a measure of agreement.

3.1 Building the earthquake catalogue

We compiled an earthquake catalogue from the USGS Comprehensive Catalogue (ComCat) for events within Greece, and a 100 km buffer around its borders to minimize edge effects, spanning January 1973 to December 2022. ComCat provides a preferred origin

and magnitude estimate for each event, which may correspond to local magnitude (M_L), coda duration magnitude (M_D), body-wave magnitude (m_b), surface-wave magnitude (M_s), or moment magnitude (M_w). The initial dataset comprised 43,196 events with a preferred magnitude ≥ 2.0 .

To ensure magnitude consistency, we converted all magnitudes to a potency magnitude, M_p , following Trugman and Ben-Zion (2024). Seismic potency (P_0) is defined as the ratio of seismic moment (M_0) to crustal rigidity (μ). Assuming a uniform crustal rigidity of 36 GPa (3.6×10^{10} N/m²), the seismic moment (in dyn-cm) is estimated from the moment magnitude (M_w) using the relation:

$$\log_{10} M_0 = 1.5 M_w + 16.1 \quad (2)$$

Seismic potency (P_0) is then calculated by:

$$\log_{10} P_0 = \log_{10} M_0 - \log_{10} \mu - 11 \quad (3)$$

with P_0 expressed in cm³, and the potency magnitude is given by:

$$M_p = (2/3) (\log_{10} P_0 + 5.4563) \quad (4)$$

When M_w was not available, M_p was estimated by converting the preferred magnitude type (M_L , m_b , M_s , or M_D) using the scaling relations of Trugman and Ben-Zion (2024), exploiting the equivalence between M_p and M_w under the assumption of uniform rigidity.

Based on the completeness analysis (Fig. S1) and to retain significant contributors to ground shaking, only events with $M_p \geq 4.5$ were used for ShakeMap generation. This resulted in a final dataset of 2,617 earthquakes over the 50-year period. Consistent with previous studies (e.g. Allen et al. 2023), the catalogue was not declustered, thereby retaining mainshocks, foreshocks, aftershocks, and triggered events, all of which may contribute to hazard exceedance. Figure 3 shows the spatial distribution of the final homogenized catalogue, while magnitude, depth, and temporal distributions are provided in Fig. S2.

3.2 Building the ShakeMap dataset

We generated ShakeMaps for all 2,617 events using the USGS ShakeMap software v4 (Worden et al. 2018, 2020). For the same period and magnitude range, only 217 ShakeMaps are available in the public USGS archive, necessitating recalculation to ensure consistency. For each event, the most up-to-date origin parameters (origin time, epicenter, depth, and magnitude) were retrieved.

Where available, strong-motion recordings and macroseismic intensity observations were incorporated to anchor the ShakeMap ground-motion fields and reduce epistemic uncertainty. In the original USGS products, such observations were available for 118 events. Additional station recordings and intensity observations for 323 earthquakes were retrieved from the National Observatory of Athens (NOA) ShakeMap database, increasing the number of observation-anchored ShakeMaps to 441. As shown in Fig. S3, ShakeMaps incorporating observational data exhibit systematically reduced uncertainty relative to fully model-based cases. Finite-source rupture models were available for 17 earthquakes; all remaining events

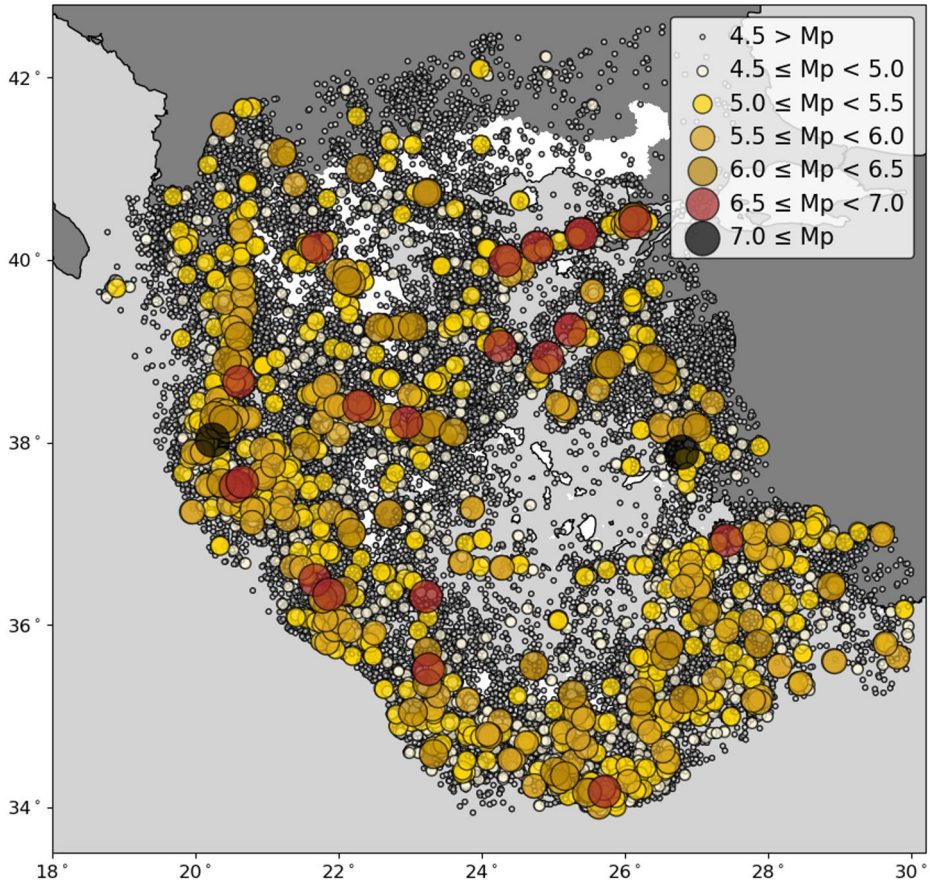


Fig. 3 Spatial distribution of the earthquake epicentres included in the final dataset used for ShakeMap generation (coloured circles), scaled according to potency magnitude (M_p), for the period January 1973 to December 2022. The final dataset comprises 2,617 events for which ShakeMaps were generated and analysed in this study. Gray circles show the epicentres of the initial earthquake catalogue (43,169 events) within a 100 km buffer around the Greek borders over the same time period, from which the final dataset was selected

were modelled as point sources with equivalent finite-fault distance corrections following Thompson and Worden (2018).

We employed three distinct ground-motion model (GMM) sets to represent active crustal, subduction interface, and subduction slab tectonic environments (Table 1), with automatic assignment based on event location and tectonic classification. For active shallow crustal earthquakes, four GMMs were used: an NGA-West model (Chiou and Youngs 2014), a global model (Cauzzi et al. 2015), a pan-European model (Akkar et al. 2014), and a locally calibrated model for Greece (Boore et al. 2021). This selection follows regional PSHA recommendations to combine global, pan-regional, and local models to represent epistemic variability without excessive model correlation. The associated weights (Table 1), derived from the GMM ranking analysis of Sotiriadis et al. (2023), define the ShakeMap logic tree and are not intended to replicate the full ESHM20 hazard-model logic tree. For subduction

Table 1 ShakeMap ground-motion modelling configuration: Ground motion models (GMMs) for three distinct tectonic models applicable to Greece: active crustal, subduction interface (SInter), and subduction slab models (SSlab)

GMMs	Weights	Tectonic Regime	Reference
AkkarEtAlRjb2014	0.12	Active Crustal	Akkar et al. (2014)
CauzziEtAl2015	0.18	Active Crustal	Cauzzi et al. (2015)
BooreEtAl2021	0.40	Active Crustal	Boore et al. (2021)
ChiouYoungs2014	0.30	Active Crustal	Chiou and Youngs (2014)
AtkinsonBoore2003SInter	0.20	Subduction Interface	Atkinson and Boore (2003)
LinLee2008SInter	0.20	Subduction Interface	Lin and Lee (2008)
AbrahamsonEtAl2015SInter	0.20	Subduction Interface	Abrahamson et al. (2016)
ZhaoEtAl2016SInter	0.40	Subduction Interface	Zhao et al. (2016)
AtkinsonBoore2003SSlab	0.20	Subduction slab	Atkinson and Boore (2003)
LinLee2008SSlab	0.20	Subduction slab	Lin and Lee (2008)
AbrahamsonEtAl2015SSlab	0.20	Subduction slab	Abrahamson et al. (2016)
ZhaoEtAl2016SSlab	0.40	Subduction slab	Zhao et al. (2016)

Weights are normalized within each tectonic regime. Rjb: denotes the Joyner–Boore distance metric used by the corresponding ground-motion models

interface and in-slab regimes, the ground-motion models and associated weights follow the default configuration implemented in the USGS ShakeMap v4 software. These weights reflect the operational logic-tree structure of ShakeMap for subduction environments and were retained here to ensure methodological consistency with the ShakeMap framework, rather than to replicate the epistemic structure of ESHM20.

Ground-motion-to-intensity conversion equations (GMICEs) and cross-correlation functions (CCFs) were selected automatically; we adopted the formulations proposed by Worden et al. (2012) and Loth and Baker (2013), respectively. For each event, we computed PGA and spectral accelerations at 0.3 s and 1.0 s. Site effects were accounted for using the USGS global Vs30 (average shear-wave velocity to 30 m depth) database (Allen and Wald 2007).

Because ESHM20 adopts the orientation-independent RotD50 metric (Boore 2006, 2010), ShakeMaps were generated directly in terms of RotD50 values. For each intensity measure, the maximum value at each grid cell across all earthquakes during the 50-year period was extracted using a regular grid of approximately 1 km resolution ($0.01^\circ \times 0.01^\circ$), comprising 143,728 cells.

To ensure consistency with the rock-site assumptions in ESHM20, we applied site amplification factors from the European Site Response Model, ESRM20 (Weatherill et al. 2021; Crowley et al. 2021), ESRM20 provides amplification factors based on topography, geology, and site condition proxies across Europe. Because the ESRM20 grid has a finer resolution ($0.008^\circ \times 0.008^\circ$) than our base grid, we adopted the median of the ESRM20 amplification factors within each base grid cell as site correction. These factors were applied uniformly to all ShakeMap-derived intensity measures. Figure 4 shows the spatial distribution of maximum PGA, Sa(0.3 s), and Sa(1.0 s) before and after conversion to rock-site conditions.

Finally, we evaluated exceedances of the ESHM20 hazard thresholds for return periods of 475 years (annual exceedance probability $\approx 0.21\%$) and 50 years (annual exceedance probability $\approx 2\%$). For each return period, we compared the ShakeMap-derived intensity measures with four ESHM20 aggregation levels (mean, 16th, 50th, and 84th percentiles), resulting in 24 exceedance tests. We did not consider longer return periods, as exceedance is expected to be negligible within a 50-year observation window (Cito et al. 2024).

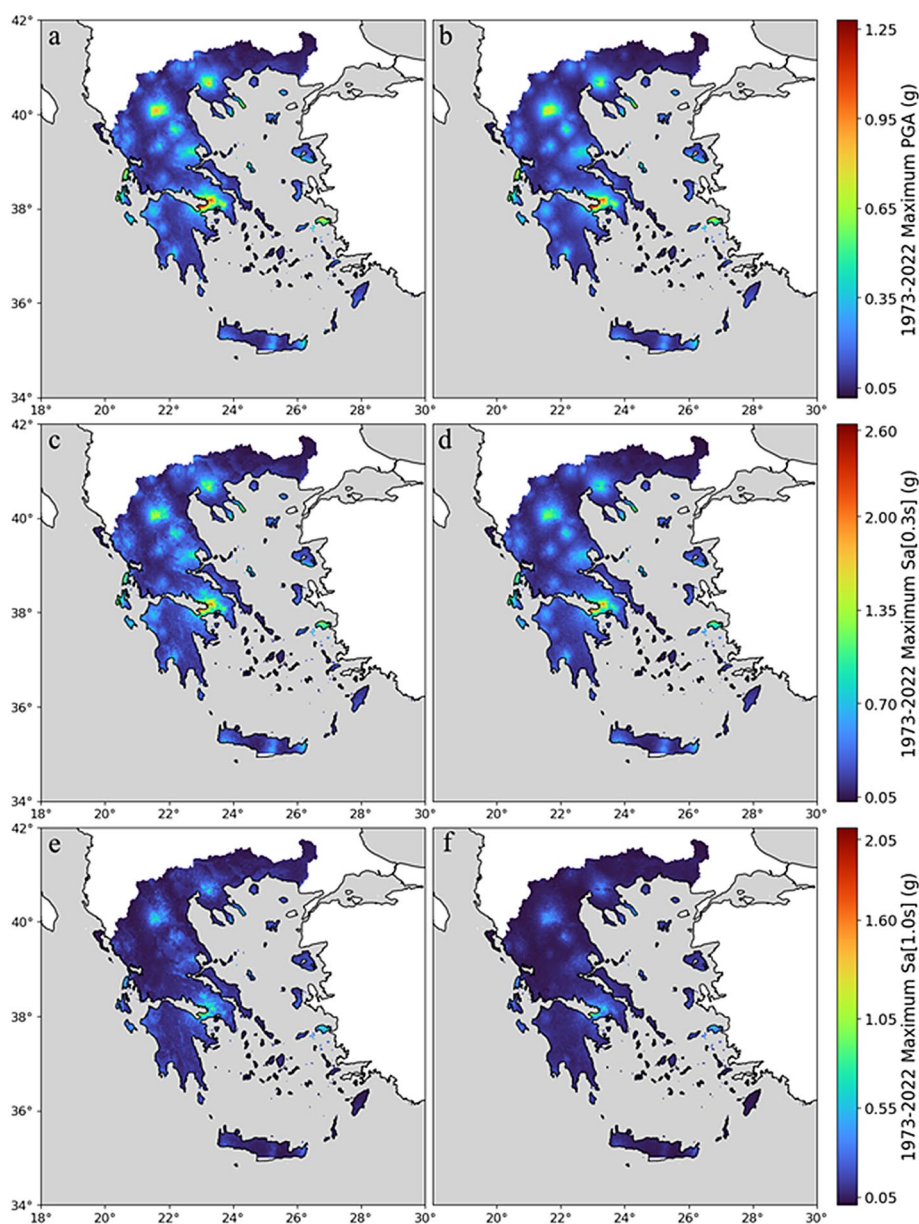


Fig. 4 Left panels (a, c, e): Spatial distribution of the maximum ShakeMap-derived RotD50 peak ground acceleration (PGA) and spectral accelerations $Sa(0.3\text{ s})$ and $Sa(1.0\text{ s})$ over the period 1973–2022 (50 years). The mapped values represent, for each grid cell, the maximum intensity across all ShakeMaps in the study period. Right panels (b, d, f): Same as left panels, but with all ShakeMap-derived intensity measures converted to rock-site conditions using amplification factors from the European Site Response Model (ESRM20; Weatherill et al. 2021; Crowley et al. 2021), ensuring consistency with ESHM20 hazard definitions

4 Results

4.1 Fractional exceedance area

The fractional exceedance area is defined as the ratio of grid cells in which the ShakeMap-derived intensity measure (IM) exceeds the corresponding ESHM20 hazard threshold to the total number of grid cells. Figure 5 shows the spatial distribution of exceedances for Peak Ground Acceleration (PGA) for the mean and the 16th, 50th, and 84th percentiles of the ESHM20 hazard levels. Figures S4 and S5 present analogous results for $S_a(0.3\text{ s})$ and $S_a(1.0\text{ s})$, respectively.

Several robust patterns are evident. Exceedances relative to $RP=50$ years generally occupy larger areas than those relative to $RP=475$ years, reflecting the lower hazard thresholds associated with shorter return periods. Exceedances relative to the 16th percentile hazard levels are spatially more extensive than those relative to the 84th percentile, consistent with the ordering of ESHM20 aggregation levels. Overall, the ShakeMap-derived exceedance patterns are largely bounded by the probabilistic envelope of ESHM20 across percentiles, while localized departures are expected given the limited 50-year time window, the hybrid nature of ShakeMap ground-motion fields, and the influence of site-response adjustments and spatial sampling of strong shaking.

Spatially, recurrent exceedances concentrate in well-known deformation zones, including the Corinth Rift, the Cephalonia Transform Fault Zone, and the northern Aegean. Additional exceedances also occur in areas of relatively lower mapped hazard. Such cases may reflect site-response effects not fully represented by V_{s30} -based adjustments, limited observation density for some events, and residual differences introduced by component conversion and rock-site normalization. Residual differences following RotD50 and rock-site adjustments are most pronounced for spectral accelerations and in regions near V_{s30} classification boundaries (Fig. S11). These effects increase local variability and can contribute to exceedance sensitivity for $S_a(0.3\text{ s})$ and $S_a(1.0\text{ s})$ compared to PGA (Figs. 5, S4, S5).

To incorporate ShakeMap uncertainty into exceedance mapping, we constructed upper and lower bounds on the ShakeMap-derived intensity measures (IMs). These bounds were obtained by shifting the maximum IM values by $\pm 1\sigma$, as provided in the ShakeMap products (expressed in natural logarithm units), prior to comparison with the ESHM20 hazard thresholds. Applying a $\pm 1\sigma$ shift in \ln space therefore corresponds to scaling the intensity measures multiplicatively in linear space by a factor of e^σ . This approach captures the sensitivity of exceedance classification for grid cells with shaking levels close to the ESHM20 hazard thresholds. Accordingly, the resulting bounds on fractional exceedance area reflect the inherent variability of ShakeMap-derived ground-motion fields rather than deterministic uncertainty limits. Table 2 summarizes these results, including the estimated exceedance areas and their associated variability.

4.2 Exceedance-count distributions and spatial dependence

To compare exceedance-count behavior with expectations implied by ESHM20, we evaluated the distributions of exceedance counts and compared them with the corresponding theoretical binomial probability mass functions (PMFs). The binomial model assumes independence among exceedances at different grid cells. In reality, earthquake ground motions

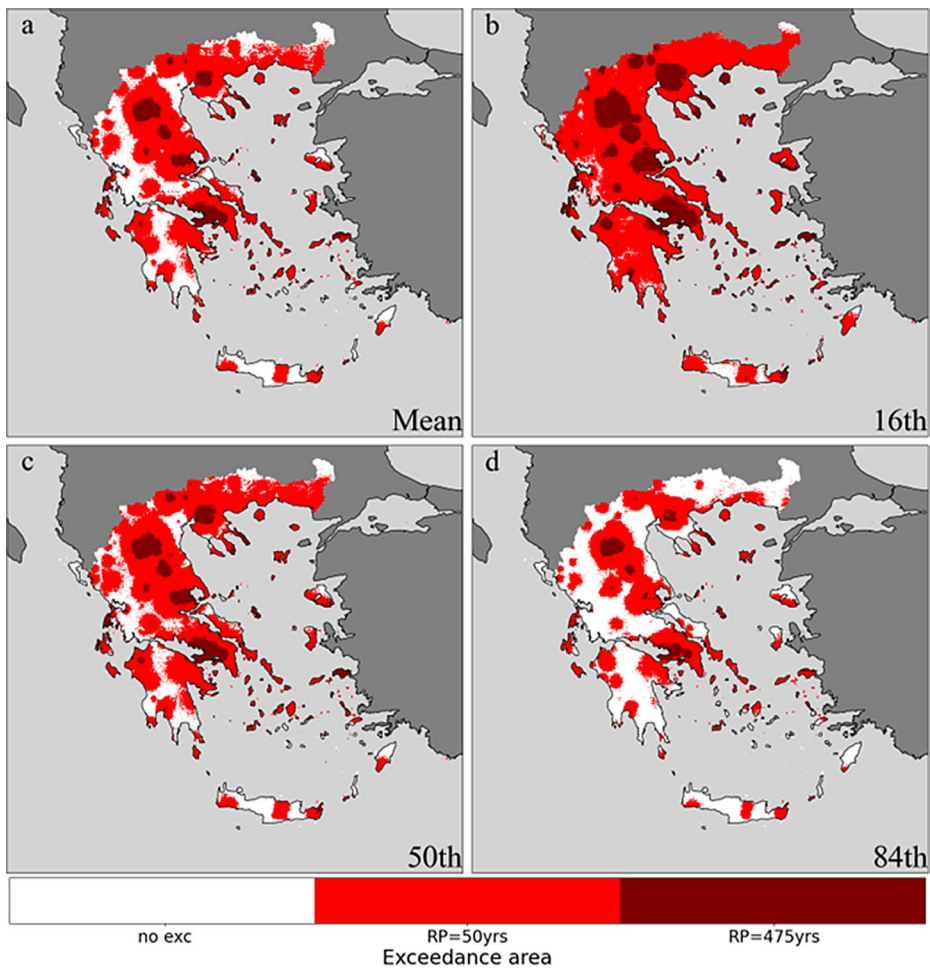


Fig. 5 Fractional exceedance areas where at least one ShakeMap-derived RotD50 peak ground acceleration (PGA) value exceeded the corresponding ESHM20 hazard threshold, for earthquakes of minimum potency magnitude 4.5, over a 50-year time window (1973–2022). Colours indicate the return period (RP) associated with the exceeded hazard level: red for RP=50 years (63.2% probability of exceedance in 50 years) and maroon for RP=475 years (10% probability of exceedance in 50 years), while white denotes no exceedance. Panels compare exceedances relative to different aggregation levels of the ESHM20 hazard model: (a) mean, (b) 16th percentile, (c) 50th percentile (median), and (d) 84th percentile. Exceedances are evaluated on ShakeMap-derived ground-motion fields adjusted to rock-site conditions and therefore represent hybrid observational–modelled outcomes rather than direct spatial observations of ground motion

are spatially correlated, such that nearby cells are likely to exhibit similar shaking levels. This spatial dependence reduces the effective number of independent samples relative to the total number of grid cells and therefore affects the interpretation of exceedance-count variability, particularly for events generating widespread strong motion. The binomial comparison is therefore used here as a first-order screening tool rather than as a formal test of statistical consistency.

Table 2 Estimated fractional exceedance area for Greece, expressed as a percentage of the national grid, for three rotation-independent intensity measures (RotD50; Boore 2006; Boore 2010) and two return periods (RP), as defined by the ESHM20 hazard maps

Return Period		Fractional Exceedance Area (%)			
RP=475 yrs	Intensity Measure	Aggregation Level	Estimated (%)	Upper bound (+1 σ) (%)	Lower bound (-1 σ) (%)
Expected Fractional Area 10%	PGA	<i>Mean</i>	7.30	22.62	2.10
		<i>16th</i>	21.20	53.99	8.12
		<i>50th</i>	9.88	29.67	3.11
		<i>84th</i>	3.91	14.06	0.88
	Sa (0.3 s)	<i>Mean</i>	6.08	23.05	1.28
		<i>16th</i>	15.23	44.23	4.56
		<i>50th</i>	7.69	26.93	1.70
		<i>84th</i>	3.25	14.42	0.51
	Sa (1.0 s)	<i>Mean</i>	8.87	30.66	2.26
		<i>16th</i>	18.00	51.41	5.44
		<i>50th</i>	10.42	34.45	2.74
		<i>84th</i>	5.40	20.97	1.09
RP=50 yrs	Intensity Measure	Aggregation Level	Estimated (%)	Upper bound (+1 σ) (%)	Lower bound (-1 σ) (%)
Expected Fractional Area 63.2%	PGA	<i>Mean</i>	66.55	97.94	28.05
		<i>16th</i>	93.79	99.97	59.90
		<i>50th</i>	74.38	98.97	34.04
		<i>84th</i>	45.00	87.67	16.46
	Sa (0.3 s)	<i>Mean</i>	60.59	95.69	24.10
		<i>16th</i>	83.11	99.23	42.59
		<i>50th</i>	65.25	96.92	27.50
		<i>84th</i>	44.47	86.51	15.46
	Sa (1.0 s)	<i>Mean</i>	71.57	95.89	30.08
		<i>16th</i>	86.27	98.85	49.74
		<i>50th</i>	74.71	96.64	33.31
		<i>84th</i>	56.92	90.93	20.22

Exceedances are computed for earthquakes with potency magnitude $M_p \geq 4.5$ during the period 1973–2022. For each intensity measure and aggregation level of the ESHM20 hazard model (mean, 16th, 50th, and 84th percentiles), the estimated fractional exceedance area is reported together with upper (+1 σ , %) and lower (-1 σ , %) bounds derived from ShakeMap uncertainty propagation. Expected fractional exceedance areas (10% for RP=475 years and 63.2% for RP=50 years) are shown for reference. Deviations from these expected values should be interpreted in the context of the limited 50-year observation window and the hybrid nature of ShakeMap-derived ground-motion fields, rather than as evidence of systematic bias in the ESHM20 hazard model

The binomial model describes the expected number of exceedances X among n independent Bernoulli outcomes with exceedance probability p , and is defined as:

$$X \sim \text{Bin}(n, p) \quad (5)$$

The probability of observing exactly k exceedances is given by the binomial probability mass function (PMF), i.e. the discrete probabilities $P(X = k)$ for $k = 0, \dots, n$:

$$P(X = k) = \binom{n}{k} p^k (1 - p)^{n-k} \quad (6)$$

In this study, the exceedance probability p is taken directly from the ShakeMap-derived fractional exceedance area (sites exposed to exceedance divided by total sites). To enable comparison on a common scale, we express exceedance counts using a percentage-based normalisation, setting $n = 100$, where each unit corresponds to 1% of the total grid-cell population. The corresponding binomial probability mass function (PMF) is then calculated using the SciPy library (Virtanen et al. 2020), representing the expected variability of exceedance fractions under the assumption of spatial independence.

To quantify similarity between the observed exceedance fractions and the corresponding binomial expectation, we compute the overlapping coefficient (OVL; Inman and Bradley 1989), defined as:

$$\text{OVL} = \int_{-\infty}^{+\infty} \min [f_1(x), f_2(x)] dx \quad (7)$$

where $f_1(x)$ represents the empirical exceedance-fraction representation and $f_2(x)$ denotes the theoretical binomial PMF. By sampling the distributions at discrete points, the integral in Eq. (7) is approximated as:

$$\text{OVL} = \sum_x \min [f_1(x), f_2(x)] \quad (8)$$

OVL values range from 0 (no overlap) to 1 (identical distributions) and are used here as a similarity metric to support comparative interpretation across intensity measures, return periods, and aggregation levels, rather than as a formal statistical test. Given the limited 50-year record relative to long return periods, OVL is applied as a pragmatic screening indicator rather than an acceptance criterion. OVL values are reported as descriptive similarity metrics to support comparative interpretation across intensity measures, return periods, and aggregation levels. No formal acceptance threshold is imposed, and the values should be interpreted in the context of the limited observation window and spatial dependence of shaking.

Figures 6 and 7 compare the empirical exceedance-count representations (black bars) with the corresponding theoretical binomial PMFs implied by the ESHM20 hazard levels (red curves), with agreement quantified using OVL. For the 475-year return period (Fig. 6), central aggregation levels (mean and 50th percentile) generally show closer agreement than the tails (16th and 84th percentiles), consistent with the ordering of hazard thresholds. For the 50-year return period (Fig. 7), exceedance patterns shift toward higher counts, reflecting the higher probability of exceedance within the observation window. Across PGA, Sa(0.3 s), and Sa(1.0 s), differences among intensity measures primarily reflect spectral-period sensitivity to site-response adjustments and the higher uncertainty sensitivity of spectral ordinates and should be interpreted through the reported OVL values rather than as categorical pass–fail outcomes.

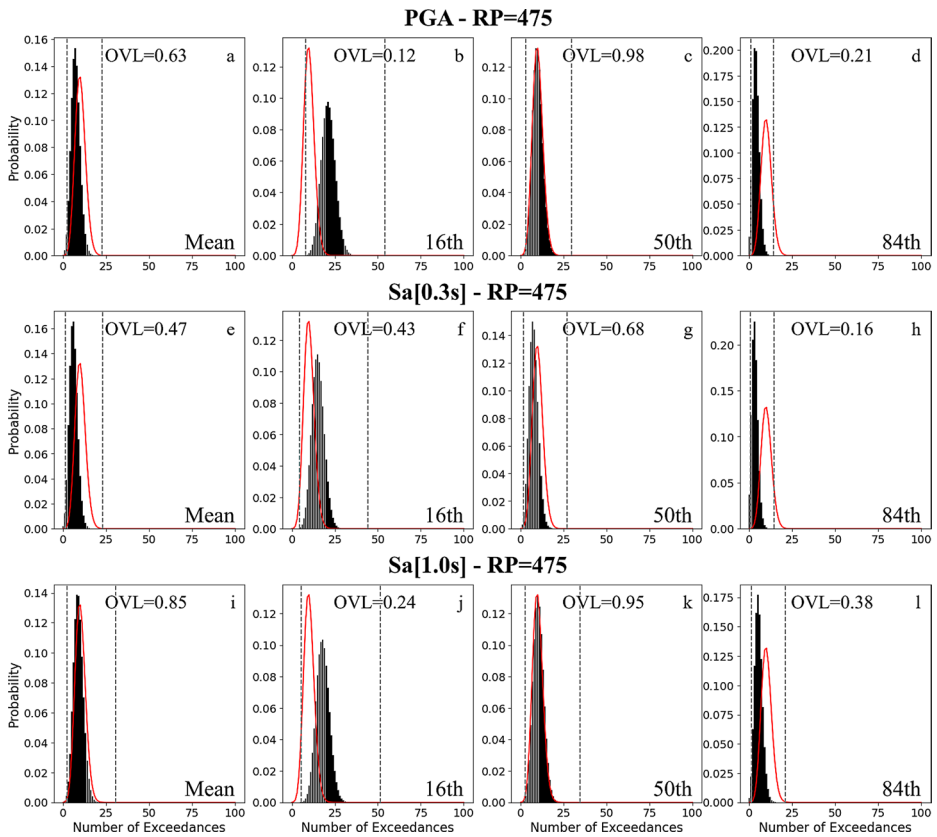


Fig. 6 Probability distributions of the number of exceedances derived from ShakeMap-based ground-motion fields (black bars) compared with the theoretical binomial distributions implied by ESHM20 hazard levels (red curves), for a return period of 475 years. Panels correspond to different ground-motion intensity measures (PGA, Sa at 0.3 s, and Sa at 1.0 s) and aggregation levels of the hazard model (mean, 16th, 50th, and 84th percentiles). Dashed vertical lines indicate the $\pm 1\sigma$ ranges of exceedance counts estimated from the ShakeMap-derived distributions. The overlapping coefficient (OVL) reported in each panel quantifies the degree of overlap between empirical and theoretical distributions, with higher values indicating closer agreement

4.3 Main contributors to exceedance

Table 3 summarizes the number of earthquakes associated with at least one exceedance of ESHM20 hazard thresholds for each intensity measure, return period, and aggregation level, and identifies the subset of exceedance-producing events for which strong-motion recordings and/or macroseismic intensity observations were available and incorporated in ShakeMap generation. Figure 8 shows the epicentral distribution of PGA exceedance-producing earthquakes, and Fig. 9 shows their magnitude and depth distributions. Figures S6–S9 provide analogous results for Sa(0.3 s) and Sa(1.0 s).

For the 475-year return period (RP), nearly all exceedance-producing earthquakes across intensity measures are associated with events that include strong-motion recordings and/or macroseismic observations (Table 3), indicating that the most influential exceedances

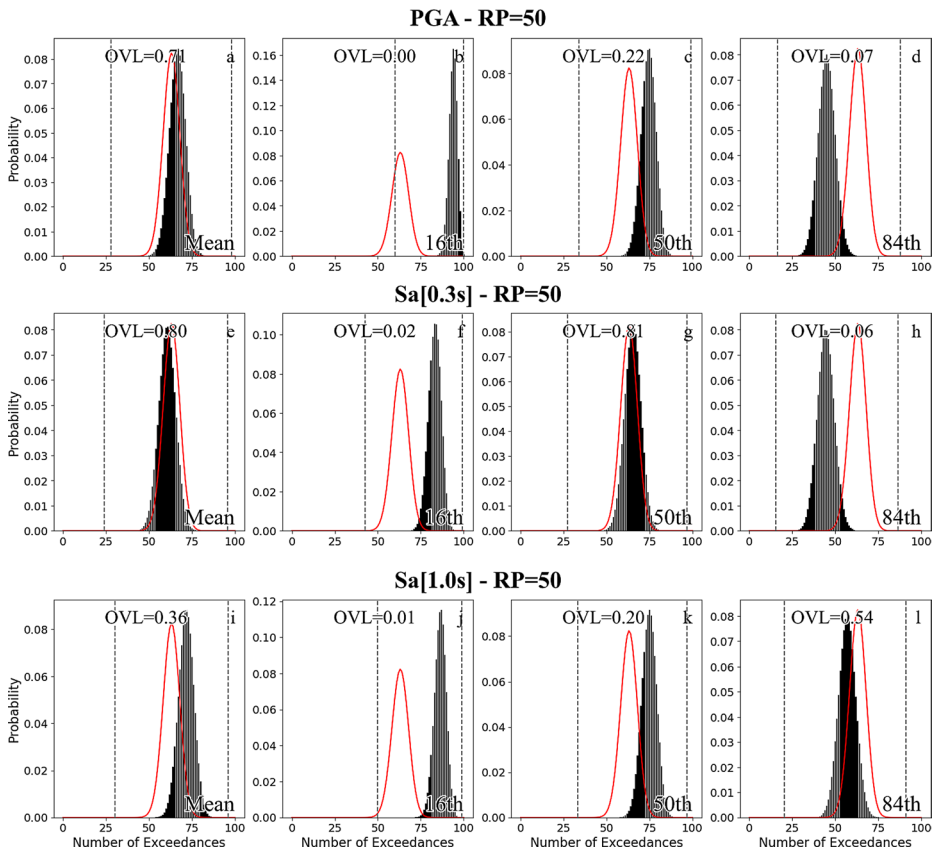


Fig. 7 As in Fig. 6 for a return period (RP) of 50 years

Table 3 Number of earthquakes that produced at least one exceedance of the ESHM20 hazard thresholds for a given intensity measure (IM) and aggregation level over the 50-year observation period (1973–2022)

Return Period	IM	Total Number of Earthquakes / with Observations			
		Mean	16th	50th	84th
RP=475 yrs	PGA	31 / 31	67 / 63	37 / 37	21 / 21
	Sa (0.3 s)	28 / 28	53 / 53	33 / 33	20 / 20
	Sa (1.0 s)	30 / 30	40 / 40	34 / 34	21 / 21
RP=50 yrs	PGA	134 / 103	153 / 110	140 / 104	98 / 89
	Sa (0.3 s)	102 / 92	124 / 101	104 / 92	93 / 87
	Sa (1.0 s)	52 / 50	57 / 55	54 / 52	49 / 48

For each case, the total number of exceedance-producing earthquakes is reported together with the number of those events for which field observations (strong-motion recordings and/or macroseismic intensity data) were available and incorporated in the ShakeMap generation. Results are shown separately for return periods of 475 and 50 years and for the mean and the 16th, 50th, and 84th percentiles of the ESHM20 hazard levels

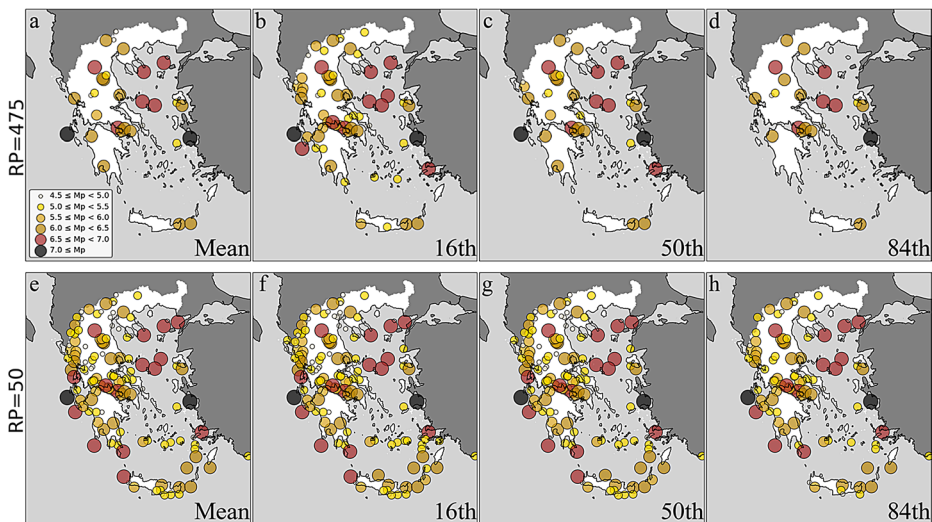


Fig. 8 Spatial distribution of earthquake epicentres (circles, coloured by potency magnitude) associated with at least one exceedance of the ESHM20 peak ground acceleration (PGA) hazard thresholds in the ShakeMap-derived ground-motion fields. Panels (a–d) correspond to exceedances relative to the 475-year return-period hazard levels, and panels (e–h) to the 50-year return-period hazard levels. Columns show different aggregation levels of the ESHM20 hazard model: (a, e) mean, (b, f) 16th percentile, (c, g) 50th percentile (median), and (d, h) 84th percentile. Exceedances are identified on ShakeMap-derived ground-motion fields adjusted to rock-site conditions

are largely observation-anchored. These exceedance-producing earthquakes are predominantly shallow crustal events with minimum magnitudes typically around $M_p \approx 4.7$, with some intermediate-depth contributions depending on spectral period and aggregation level. For $RP=50$ years, exceedances extend across the full magnitude range down to $M_p=4.5$, except for $S_a(1.0\text{ s})$, for which exceedance onset occurs at higher magnitudes (approximately $M_p \approx 5.1$). The spatial distribution of exceedance-producing earthquakes is consistent with the primary deformation zones of Greece, including the HSZ, the Corinth Rift, and the extensional domains of the Aegean, reflecting the combined influence of seismotectonic setting, source characteristics, and site-response representation.

4.4 Sensitivity to modelling choices

A sensitivity analysis was conducted by recalculating ShakeMaps for selected events using alternative ground-motion models, including the Kotha et al. (2020) used as a backbone GMM in ESHM20 and the locally calibrated Boore et al. (2021). The resulting distance-dependent IM behaviour (Fig. S10) illustrates the scale of model-dependent variability, particularly in the near-field.

Additional supplementary analyses compared ESRM20-based rock-site corrections with empirical amplification factors following Borchardt (1994). Differences are most evident near Eurocode 8 Vs30 class boundaries (Fig. S11), consistent with increased sensitivity of site-response parameterisation in transitional ranges. Finally, component-definition effects were assessed by comparing RotD50 with greater-of-two-horizontal IMs. While regional

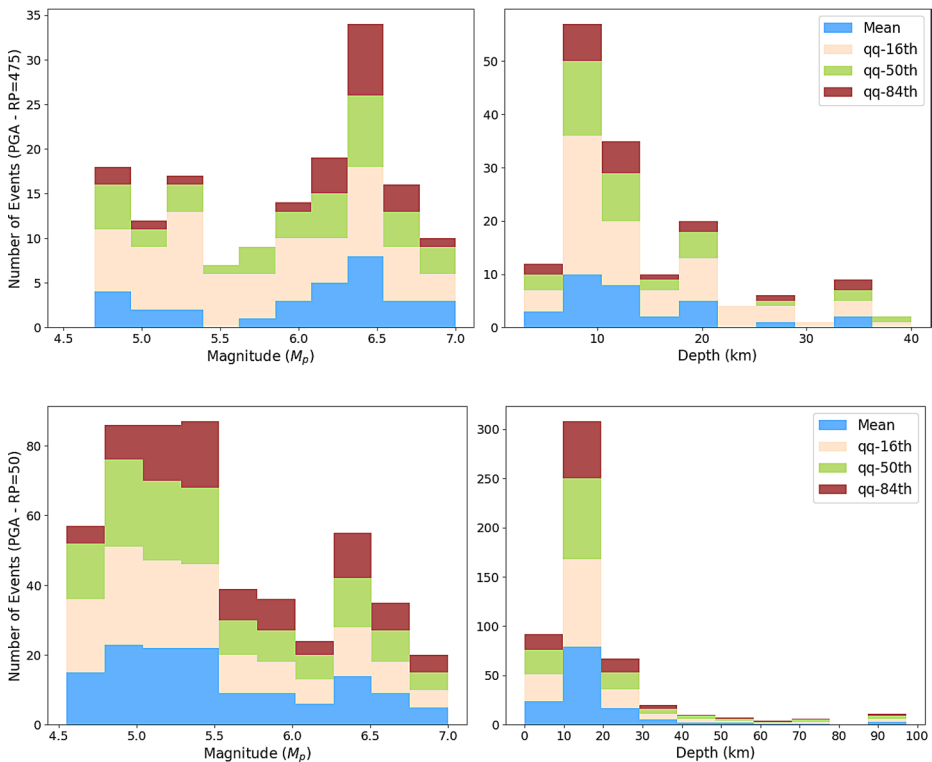


Fig. 9 Number of earthquake events associated with at least one exceedance of the ESHM20 peak ground acceleration (PGA) hazard thresholds in the ShakeMap-derived ground-motion fields, shown as a function of potency magnitude (left panels) and focal depth (right panels). Top panels correspond to exceedances relative to the 475-year return-period hazard levels, and bottom panels to the 50-year return-period hazard levels. Coloured bars represent exceedance counts relative to different aggregation levels of the ESHM20 hazard model (mean, 16th percentile, 50th percentile, and 84th percentile)

differences are limited, local effects can be substantial near large earthquake epicentres (Table S1; Fig. S12), supporting the use of RotD50 for consistency with ESHM20.

5 Conclusions

Analysis of 2,617 ShakeMaps indicates that the 2020 European Seismic Hazard Model (ESHM20) produces hazard levels for Greece that are broadly consistent with ShakeMap-derived ground-motion fields, particularly for central aggregation levels and for peak ground acceleration. The analysis is based on hybrid ground-motion fields that combine observational constraints with model-based spatial interpolation. Strong-motion recordings and/or macroseismic intensity observations were incorporated for 441 earthquakes, and exceedance-producing events—especially for the 475-year return period—are predominantly associated with these observation-anchored cases. This reduces the likelihood that exceedance patterns arise solely from ground-motion model extrapolation and supports their interpretation as physically plausible outcomes within the expected variability of regional shaking.

Exceedance comparisons for the 475-year return period must nevertheless be interpreted with caution. A 50-year observational window provides limited statistical power for evaluating hazard levels associated with rare events, even when observation-anchored fields are available. This limitation is intrinsic to empirical assessments of long-return-period hazard and does not imply inadequacy of the hazard model. Accordingly, exceedance statistics at $RP=475$ years are best regarded as indicative consistency measures rather than as quantitative tests of hazard-model accuracy.

At the same time, the spatial intensity measures evaluated on the national grid remain influenced by the ShakeMap modelling chain, including ground-motion models, site-condition adjustments, and interpolation assumptions. The results should therefore be interpreted as outcomes of a structured consistency screening exercise rather than as direct spatial validation of hazard levels.

Overall, the agreement observed between ShakeMap-derived exceedance fractions and ESHM20 hazard expectations across intensity measures, aggregation levels, and return periods supports the internal coherence of the hazard model when confronted with a 50-year record of ground shaking. Remaining discrepancies are consistent with recognised sources of epistemic uncertainty, including ground-motion model variability, site-response representation, and spatial correlation of shaking. The framework presented here provides a transparent and reproducible basis for national-scale evaluation of regional seismic hazard model behaviour.

Supplementary Information The online version contains supplementary material available at <https://doi.org/10.1007/s10518-026-02429-5>.

Acknowledgements The authors gratefully acknowledge the constructive comments and suggestions provided by Laurentiu Danciu and an anonymous reviewer, which helped to improve the clarity and overall quality of the manuscript. The authors also thank the Editor for handling the review process.

Author contributions All authors contributed to the study conception and design. Material preparation, data collection, and analysis were performed by N.A.K., who also wrote the first draft of the manuscript. All authors reviewed and approved the final manuscript.

Funding Open access funding provided by HEAL-Link Greece. This work has received funding from the European Union's Horizon Europe research and innovation program under grant agreement No. 101136217 (COREu). A.K. also acknowledges partial financial support from the European Union's Horizon Europe INFRA-2023-DEV-01 program under grant agreement No. 101131592 (EPOS-ON). Open-access funding was provided by the Aristotle University of Thessaloniki.

Data availability The USGS Comprehensive Catalogue (ComCat) is available at <https://earthquake.usgs.gov/data/comcat/>. The National Observatory of Athens (NOA) ShakeMap database is available at <https://accenet.gein.noa.gr/shakemaps>. The NOFAULTS v6 dataset is available at Zenodo (<https://doi.org/10.5281/zenodo.3483135>). The USGS global slope-based Vs30 database is available at <https://earthquake.usgs.gov/data/vs30/>. The ESHM20 hazard maps (<https://doi.org/10.12686/a15>) are accessible through the EPOS Data Portal at <https://www.epos-eu.org/dataportal> and the EFEHR GitLab repository at <https://gitlab.seismo.ethz.ch/efehr/eshm20>. Data and tools related to the European Site Response Model (ESRM20) are available at <https://nextcloud.gfz.de/s/93ZR4ky8D4mDXb9> and https://gitlab.seismo.ethz.ch/efehr/esrm20_sitemodel, respectively. All data products generated in this study, will be archived at the COREu project Open Research Repository <https://zenodo.org/communities/coreu/records?q=%26list%26p=1%26s=10>. All links were last accessed on 17 December 2025.

Declarations

Competing interests The authors declare that they have no competing financial or non-financial interests.

Open Access This article is licensed under a Creative Commons Attribution 4.0 International License, which permits use, sharing, adaptation, distribution and reproduction in any medium or format, as long as you give appropriate credit to the original author(s) and the source, provide a link to the Creative Commons licence, and indicate if changes were made. The images or other third party material in this article are included in the article's Creative Commons licence, unless indicated otherwise in a credit line to the material. If material is not included in the article's Creative Commons licence and your intended use is not permitted by statutory regulation or exceeds the permitted use, you will need to obtain permission directly from the copyright holder. To view a copy of this licence, visit <http://creativecommons.org/licenses/by/4.0/>.

References

- Abrahamson N, Gregor N, Addo K (2016) BC Hydro ground motion prediction equations for subduction earthquakes. *Earthq Spectra* 32(1):23–44. <https://doi.org/10.1193/051712EQS188MR>
- Akkar S, Sandikkaya MA, Bommer JJ (2014) Empirical ground-motion models for point- and extended-source crustal earthquake scenarios in Europe and the Middle East. *Bull Earthq Eng* 12(1):359–387. <https://doi.org/10.1007/s10518-013-9461-4>
- Albareello D, D'Amico V (2008) Testing probabilistic seismic hazard estimates by comparison with observations: an example in Italy. *Geophys J Int* 175(3):1088–1094. <https://doi.org/10.1111/j.1365-246X.2008.03928.x>
- Allen TI, Wald DJ (2007) Topographic slope as a proxy for seismic site conditions and amplification. *Bull Seismol Soc Am* 97(5):1379–1395. <https://doi.org/10.1785/0120060267>
- Allen TI, Wald DJ, Earle PS, Marano KD, Hotovec AJ, Lin K, Hearne MG (2009) An atlas of ShakeMaps and population exposure catalog for earthquake loss modeling. *Bull Earthq Eng* 7(3):701–718. <https://doi.org/10.1007/s10518-009-9120-y>
- Allen TI, Ghasemi H, Griffin JD (2023) Exploring Australian hazard map exceedance using an atlas of historical ShakeMaps. *Earthq Spectra* 39(2):985–1006. <https://doi.org/10.1177/87552930231151977>
- Atkinson GM, Boore DM (2003) Empirical ground-motion relations for subduction-zone earthquakes and their application to Cascadia and other regions. *Bull Seismol Soc Am* 93(4):1703–1729. <https://doi.org/10.1785/0120020156>
- Boore DM (2006) Orientation-independent measures of ground motion. *Bull Seismol Soc Am* 96(4A):1502–1511. <https://doi.org/10.1785/0120050209>
- Boore DM (2010) Orientation-independent, nongeometric-mean measures of seismic intensity from two horizontal components of motion. *Bull Seismol Soc Am* 100(4):1830–1835. <https://doi.org/10.1785/0120090400>
- Boore DM, Stewart JP, Skarlatoudis A, Seyhan E, Margaris B, Theodoulidis N, Scordilis E, Kalogeras I, Klimis N, Melis N (2021) A ground-motion prediction model for shallow crustal earthquakes in Greece. *Bull Seismol Soc Am* 111(5):2505–2531. <https://doi.org/10.1785/0120200270>
- Borcherdt RD (1994) Estimates of site-dependent response spectra for design (methodology and justification). *Earthq Spectra* 10(4):617–653. <https://doi.org/10.1193/1.1585791>
- Cauzzi C, Faccioli E, Vanini M, Bianchini A (2015) Updated predictive equations for broadband (0.01–10 s) horizontal response spectra and peak ground motions, based on a global dataset of digital acceleration records. *Bull Earthq Eng* 13(6):1587–1612. <https://doi.org/10.1007/s10518-014-9685-y>
- CEN (2004) Eurocode 8: design provisions for earthquake resistance of structures—Part 1: general rules, seismic actions and rules for buildings, EN 1998-1. European Committee for Standardization, Brussels
- Chiou BSJ, Youngs RR (2014) Update of the Chiou and Youngs NGA model for the average horizontal component of peak ground motion and response spectra. *Earthq Spectra* 30(3):1117–1153. <https://doi.org/10.1193/072813EQS219M>
- Chousianitis K, Sboras S, Mouslopoulou V, Chouliaras G, Hristopoulos DT (2024) The upper crustal deformation field of Greece inferred from GPS data and its correlation with earthquake occurrence. *J Geophys Res Solid Earth* 129:e2023JB028004. <https://doi.org/10.1029/2023JB028004>
- Cito P, Vitale A, Iervolino I (2024) Territorial exceedance of probabilistic seismic hazard from ShakeMap data. *Sci Rep* 14:4840. <https://doi.org/10.1038/s41598-024-55415-9>

- Crowley H, Dabbeek J, Despotaki V, Rodrigues D, Martins L, Silva V, Romão X, Pereira N, Weatherill G, Danciu L (2021) European seismic risk model (ESRM20). EFERH Tech Rep 002. <https://doi.org/10.7414/EUC-EFERH-TR002-ESRM20>
- Danciu L, Nandan S, Reyes C, Basili R, Weatherill G, Beauval C, Rovida A, Vilanova S, Sesetyan K, Bard PY, Cotton F, Wiener S, Giardini D (2021) The 2020 update of the European Seismic Hazard Model: model overview. *Bull Earthq Eng* 19(6):2545–2562. <https://doi.org/10.12686/a15>
- Ganas A, Oikonomou IA, Tsimi C (2013) NOFAULTS: a digital database for active faults in Greece. *Bull Geol Soc Greece* 47(2):518–530. <https://doi.org/10.12681/bgsg.11079>
- Giardini D, Grünthal G, Shedlock KM, Zhang P (1999) The GSHAP global seismic hazard map. *Ann Geofis* 42(6):1225–1230
- Inman HF, Bradley EL (1989) The overlapping coefficient as a measure of agreement between probability distributions and point estimation of the overlap of two normal densities. *Commun Stat Theory Methods* 18(10):3851–3874. <https://doi.org/10.1080/03610928908830127>
- Jolivet L, Faccenna C, Huet B et al (2013) Aegean tectonics: strain localisation, slab tearing and trench retreat. *Tectonophysics* 597–598:1–33. <https://doi.org/10.1016/j.tecto.2012.06.011>
- Kaviris G, Zymvragakis A, Bonatis P, Sakkas G, Kouskouna V, Voulgaris N (2022) Probabilistic seismic hazard assessment for the broader Messinia (SW Greece) region. *Pure Appl Geophys* 179(10):3711–3732. <https://doi.org/10.1007/s00024-022-02950-z>
- Kiratzi A (2002) Stress tensor inversions along the westernmost North Anatolian Fault Zone and its continuation into the North Aegean Sea. *Geophys J Int* 151(2):360–376
- Kotha SR, Weatherill G, Bindi D, Cotton F (2020) A regionally adaptable ground-motion model for shallow crustal earthquakes in Europe. *Bull Earthq Eng* 18(9):4091–4125. <https://doi.org/10.1007/s10518-020-00869-1>
- Le Pichon X, Angelier J (1979) The Hellenic Arc and Trench System: a key to the neotectonic evolution of the Eastern Mediterranean area. *Tectonophysics* 60(1–2):1–42. [https://doi.org/10.1016/0040-1951\(79\)90131-8](https://doi.org/10.1016/0040-1951(79)90131-8)
- Lin PS, Lee CT (2008) Ground-motion attenuation relationships for subduction-zone earthquakes in north-eastern Taiwan. *Bull Seismol Soc Am* 98(1):220–240. <https://doi.org/10.1785/0120060002>
- Loth C, Baker JW (2013) A spatial cross-correlation model of spectral accelerations at multiple periods. *Earthq Eng Struct Dyn* 42(3):397–417. <https://doi.org/10.1002/eqe.2212>
- Manea EF, Danciu L, Cioflan CO, Toma-Danila D, Gerstenberger M (2024) Testing the 2020 European Seismic Hazard Model against observations from Romania. *Nat Hazards Earth Syst Sci* 24:1–18. <https://doi.org/10.5194/nhess-2023-232>
- Marzocchi W, Meletti C, D'Amico V, Lanzano G, Luzi L, Martinelli F et al (2025) Guidelines for the scientific evaluation of a national seismic hazard model: the legacy of the MPS19 Italian model. *Bull Seismol Soc Am* 115(6):2826–2844. <https://doi.org/10.1785/0120240248>
- Papazachos C, Papaioannou C, Papastamatiou D, Margaris B, Theodoulidis N (1990) On the reliability of different methods of seismic hazard assessment in Greece. *Nat Hazards* 3(2):141–151. <https://doi.org/10.1007/BF00140428>
- Pothon A, Gueguen P, Buisine S, Bard PY (2020) Comparing probabilistic seismic hazard maps with Shake-Map footprints for Indonesia. *Seismol Res Lett* 91(3):1461–1473. <https://doi.org/10.1785/0220190171>
- Reilinger R, McClusky S, Paradissis D, Ergintav S, Vernant P (2010) Geodetic constraints on the tectonic evolution of the Aegean region and strain accumulation along the Hellenic subduction zone. *Tectonophysics* 488(1–4):22–30. <https://doi.org/10.1016/j.tecto.2009.05.027>
- Rey J, Beauval C, Douglas J (2018) Do French macroseismic intensity observations agree with expectations from the European Seismic Hazard Model 2013? *J Seismol* 22(1):119–134. <https://doi.org/10.1007/s10950-017-9724-7>
- Slejko D, Santulin M, Garcia Pelaez J et al (2010) Preliminary seismic hazard assessments for the area of Pylos and surrounding region (SW Peloponnese). *Boll Geofis Teor Appl* 51:163–186
- Slejko D, Rebez A, Santulin M et al (2021) Seismic hazard for the Trans Adriatic Pipeline (TAP). Part 1: probabilistic seismic hazard analysis along the pipeline. *Bull Earthq Eng* 19(9):3349–3388. <https://doi.org/10.1007/s10518-021-01111-2>
- Sotiriadis D, Margaris B, Klimis N, Dokas IM (2023) Seismic hazard in Greece: a comparative study for the region of East Macedonia and Thrace. *GeoHazards* 4(3):239–266. <https://doi.org/10.3390/geohazards4030014>
- Stylianou EG, Kouskouna V, Papoulia J (2016) Seismic hazard assessment in the North Aegean Trough based on a new seismogenic zonation. *Bull Geol Soc Greece* 50:1463–1475. <https://doi.org/10.12681/bgsg.38198>
- Tasan H, Beauval C, Helmstetter A, Sandikkaya MA, Guéguen P (2014) Testing probabilistic seismic hazard estimates against accelerometric data in two countries: France and Turkey. *Geophys J Int* 198(3):1554–1571. <https://doi.org/10.1093/gji/ggu191>

- Thompson EM, Worden CB (2018) Estimating rupture distances without a rupture. *Bull Seismol Soc Am* 108(1):371–379. <https://doi.org/10.1785/0120170174>
- Trugman DT, Ben-Zion Y (2024) Potency–magnitude scaling relations and a unified earthquake catalog for the western United States. *Seismol Rec* 4(3):223–230. <https://doi.org/10.1785/0320240022>
- Tsapanos T, Mäntyniemi P, Kijko A (2009) A probabilistic seismic hazard assessment for Greece and the surrounding region including site-specific considerations. *Ann Geophys* 52(6):739–752. <https://doi.org/10.4401/ag-3367>
- Tselentis GA, Danciu L (2010) Probabilistic seismic hazard assessment in Greece – Part 1: engineering ground motion parameters. *Nat Hazards Earth Syst Sci* 10:25–39. <https://doi.org/10.5194/nhess-10-25-2010>
- Vamvakaris D, Papazachos C, Papaioannou C, Scordilis E, Karakaisis G (2017) Seismic hazard assessment in the broader Aegean area using time-independent seismicity models based on synthetic earthquake catalogs. *Bull Geol Soc Greece* 50:1463–1478. <https://doi.org/10.12681/bgsg.11859>
- Vavlas N, Kiratzi A, Margaritis B, Karakaisis G (2019) Probabilistic seismic hazard assessment for Lesbos Island using the logic-tree approach. *Bull Geol Soc Greece* 55(1):109–136. <https://doi.org/10.12681/bgsg.20705>
- Virtanen P, Gommers R, Oliphant TE et al (2020) SciPy 1.0: fundamental algorithms for scientific computing in Python. *Nat Methods* 17:261–272. <https://doi.org/10.1038/s41592-019-0686-2>
- Weatherill GA, Crowley H, Roullé A et al (2021) European site response model datasets viewer (v1.0). <https://doi.org/10.7414/EUC-EUROPEAN-SITE-MODEL-DATA-VIEWER>
- Woessner J, Danciu L, Giardini D et al (2015) The 2013 European Seismic Hazard Model: key components and results. *Bull Earthq Eng* 13(12):3553–3596. <https://doi.org/10.1007/s10518-015-9795-1>
- Worden CB, Gerstenberger MC, Rhoades DA, Wald DJ (2012) Probabilistic relationships between ground-motion parameters and Modified Mercalli intensity in California. *Bull Seismol Soc Am* 102(1):204–221. <https://doi.org/10.1785/0120110156>
- Worden CB, Hearne M, Thompson E (2018) ShakeMap v4 software. <https://doi.org/10.5066/P97FHE0I>
- Worden CB, Thompson EM, Hearne M, Wald DJ (2020) ShakeMap manual online: technical manual, user’s guide, and software guide. <https://doi.org/10.5066/F7D21VPQ>
- Zhao JX, Jiang F, Shi P et al (2016) Ground-motion prediction equations for subduction slab earthquakes in Japan using site class and simple geometric attenuation functions. *Bull Seismol Soc Am* 106(4):1511–1534. <https://doi.org/10.1785/0120150056>

Publisher’s note Springer Nature remains neutral with regard to jurisdictional claims in published maps and institutional affiliations.

APPENDIX

Table S1: Estimated fractional exceedance areas (%) for Greece based on three intensity measures (IMs) computed using the greater-of-two-horizontal components, as typically reported in USGS ShakeMaps, for two return periods (RP) according to the ESHM20 hazard maps. Results are shown for earthquakes with minimum potency magnitude $M_p \geq 4.5$ occurring during the period 1973–2022. For each intensity measure and aggregation level of the ESHM20 hazard model (mean, 16th, 50th, and 84th percentiles), the estimated fractional exceedance area is reported together with upper ($+1\sigma$) and lower (-1σ) bounds derived from ShakeMap uncertainty propagation. These bounds reflect the effect of ShakeMap uncertainty on exceedance mapping when using the greater-of-two-horizontals component definition and are provided for comparison with the RotD50-based results presented in the main text.

			Fractional Exceedance Area (%)		
	Intensity Measure	Aggregation Level	Estimated (%)	Upper bound ($+1\sigma$) (%)	Lower bound (-1σ) (%)
RP = 475 yrs Expected Fractional Area 10%	PGA	Mean	6.06	16.50	1.93
		16th	16.84	43.17	6.89
		50th	7.85	22.19	2.77
		84th	3.43	10.01	0.90
	Sa (0.3 s)	Mean	5.38	19.38	1.27
		16th	13.36	37.78	4.17
		50th	6.78	22.73	1.62
		84th	2.95	12.04	0.55
	Sa (1.0 s)	Mean	7.79	28.07	2.09
		16th	16.38	47.56	4.81
		50th	9.30	31.63	2.46
		84th	4.77	18.86	1.04
RP = 50 yrs Expected Fractional Area 63.2%	Intensity Measure	Aggregation Level	Estimated (%)	Upper bound ($+1\sigma$) (%)	Lower bound (-1σ) (%)
	PGA	Mean	56.27	94.74	23.31
		16th	89.25	99.84	51.81
		50th	65.08	97.13	28.25
		84th	35.64	79.41	13.94
	Sa (0.3 s)	Mean	54.08	92.30	21.36
		16th	78.36	98.23	38.09
		50th	58.89	94.06	24.35
		84th	39.05	81.08	13.77
	Sa (1.0 s)	Mean	68.10	94.45	27.87
		16th	83.58	98.16	46.48
		50th	71.43	95.42	30.98
		84th	52.94	88.22	18.45

Appendix Figures:

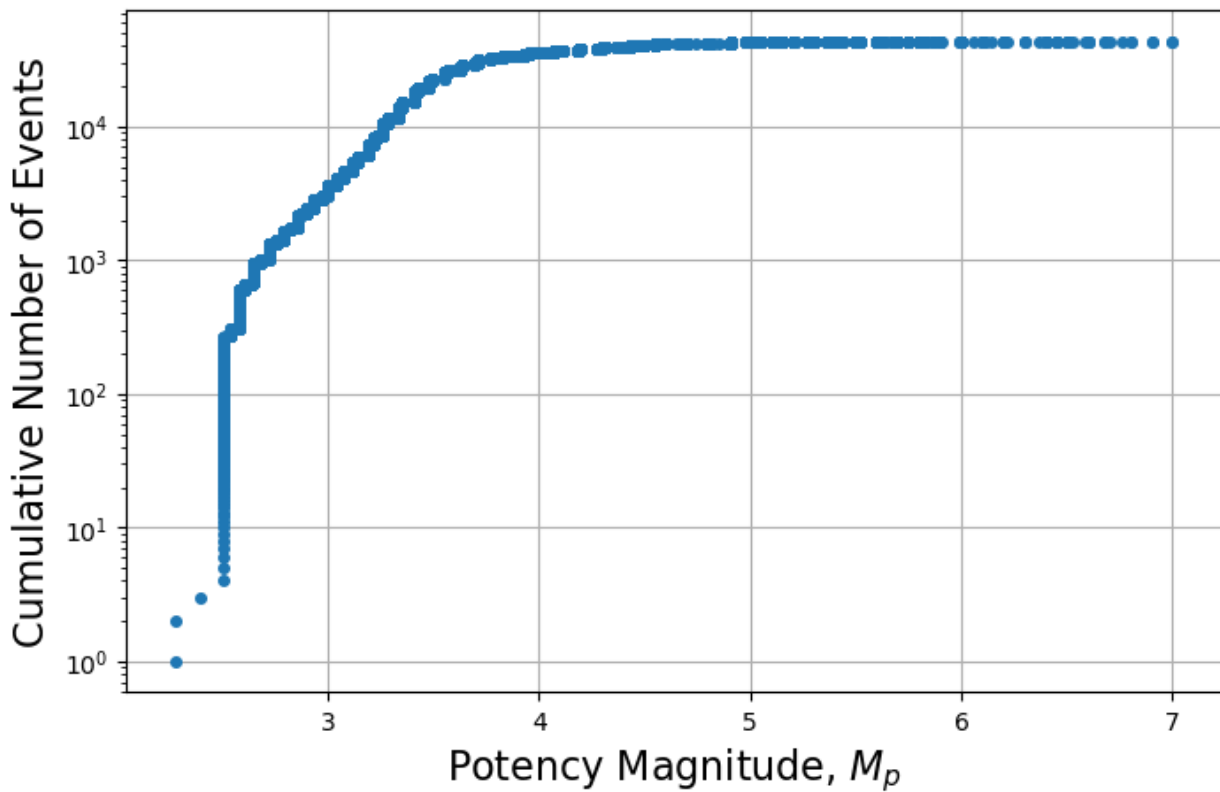


Figure S1. Cumulative frequency-magnitude distribution of the USGS ComCat catalogue used in this study for earthquakes occurring between January 1973 and December 2022 (43,196 events). A threshold potency magnitude of $M_p \geq 4.5$ is adopted for the analyses, corresponding to the minimum magnitude above which ShakeMaps are generated, and exceedance statistics are evaluated.

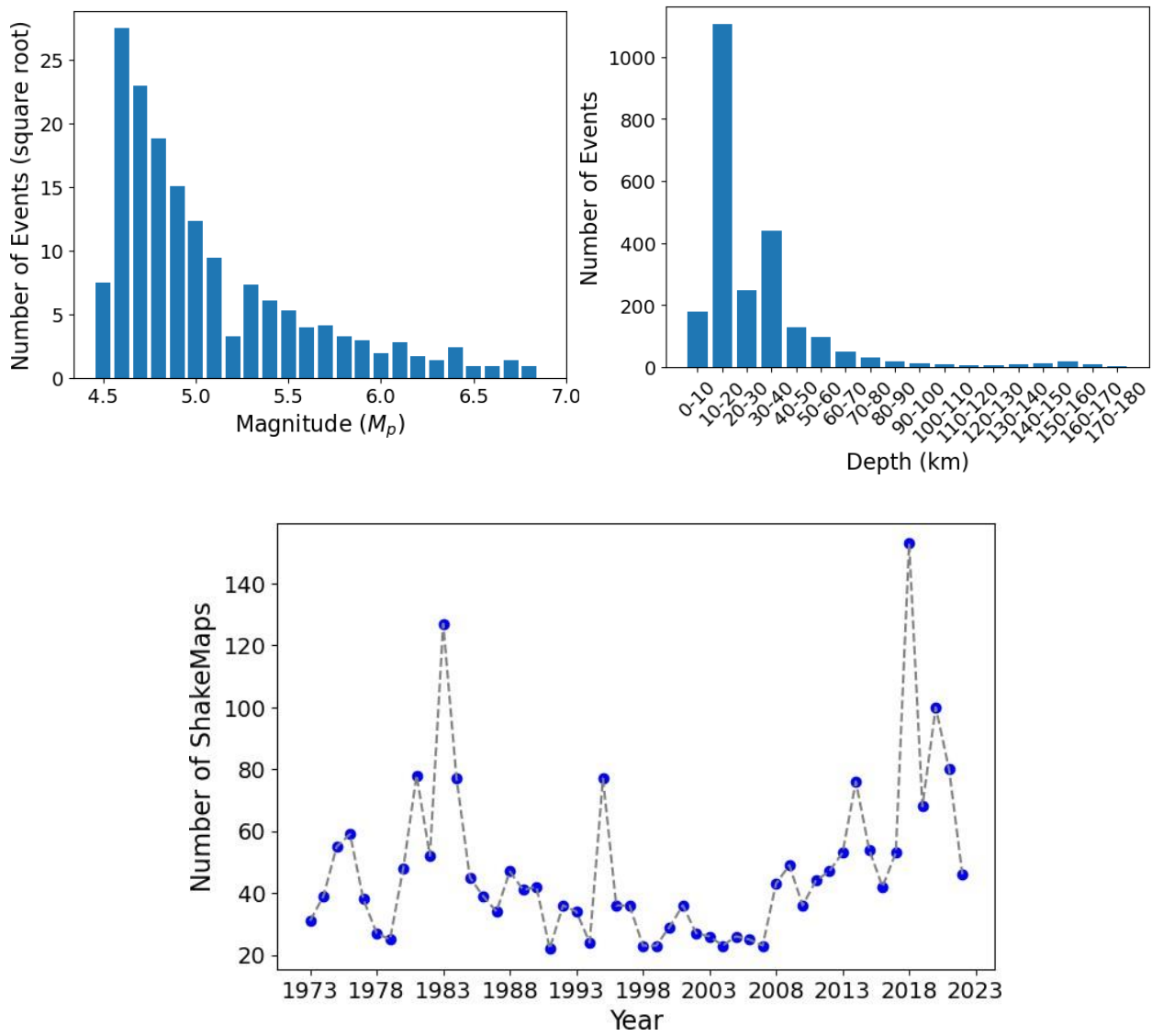


Figure S2. Distributions of the 2,617 ShakeMap footprints analysed in this study for the period January 1973 to December 2022: (a) potency magnitude (M_p), (b) focal depth, and (c) annual number of ShakeMaps. The magnitude distribution reflects the decreasing frequency of larger events, while the depth distribution is dominated by shallow earthquakes, with fewer intermediate-depth events. The annual counts illustrate temporal variability in ShakeMap availability over the study period.

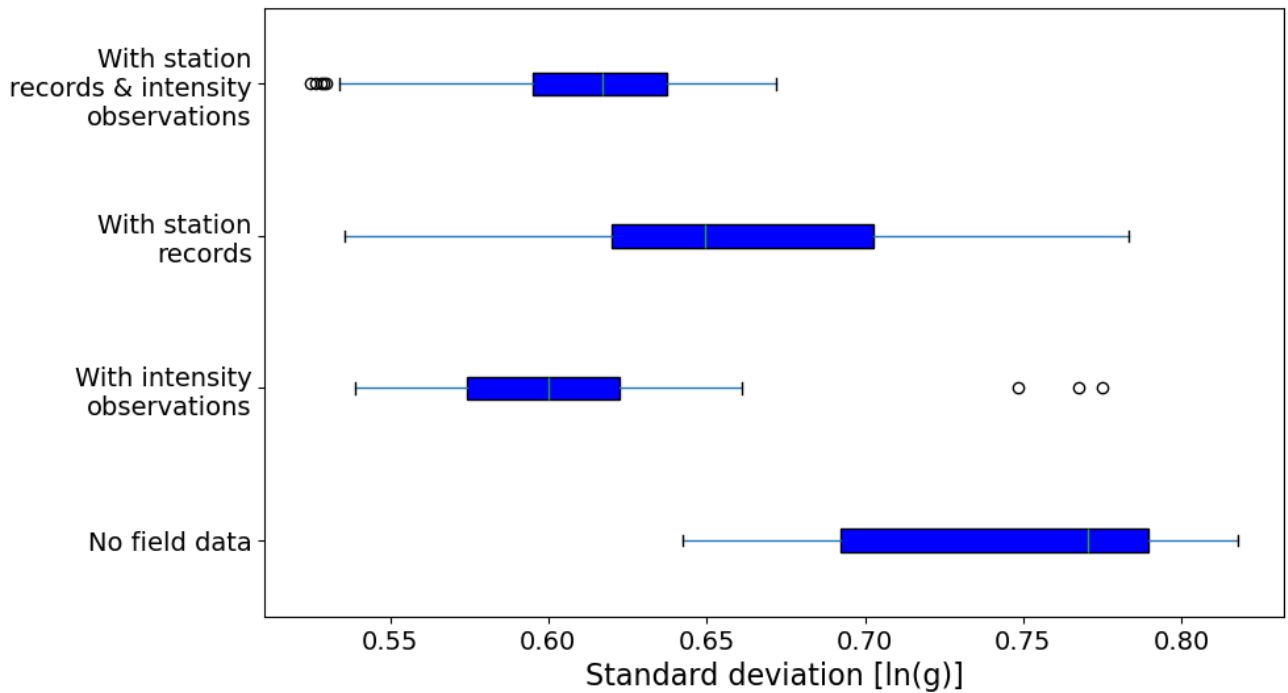


Figure S3. Boxplot representation of the distribution of the mean standard deviation of ShakeMap-derived peak ground acceleration (PGA), expressed in $\ln(g)$, across the 2,617 ShakeMap footprints analysed in this study. For each ShakeMap, the standard deviation is averaged over the spatial grid. Boxes indicate the interquartile range (25th–75th percentiles), the central line denotes the median, whiskers extend to 1.5 times the interquartile range, and circles represent outliers. Distributions are shown separately for ShakeMaps incorporating strong-motion station recordings and/or macroseismic intensity observations and for ShakeMaps without field data.

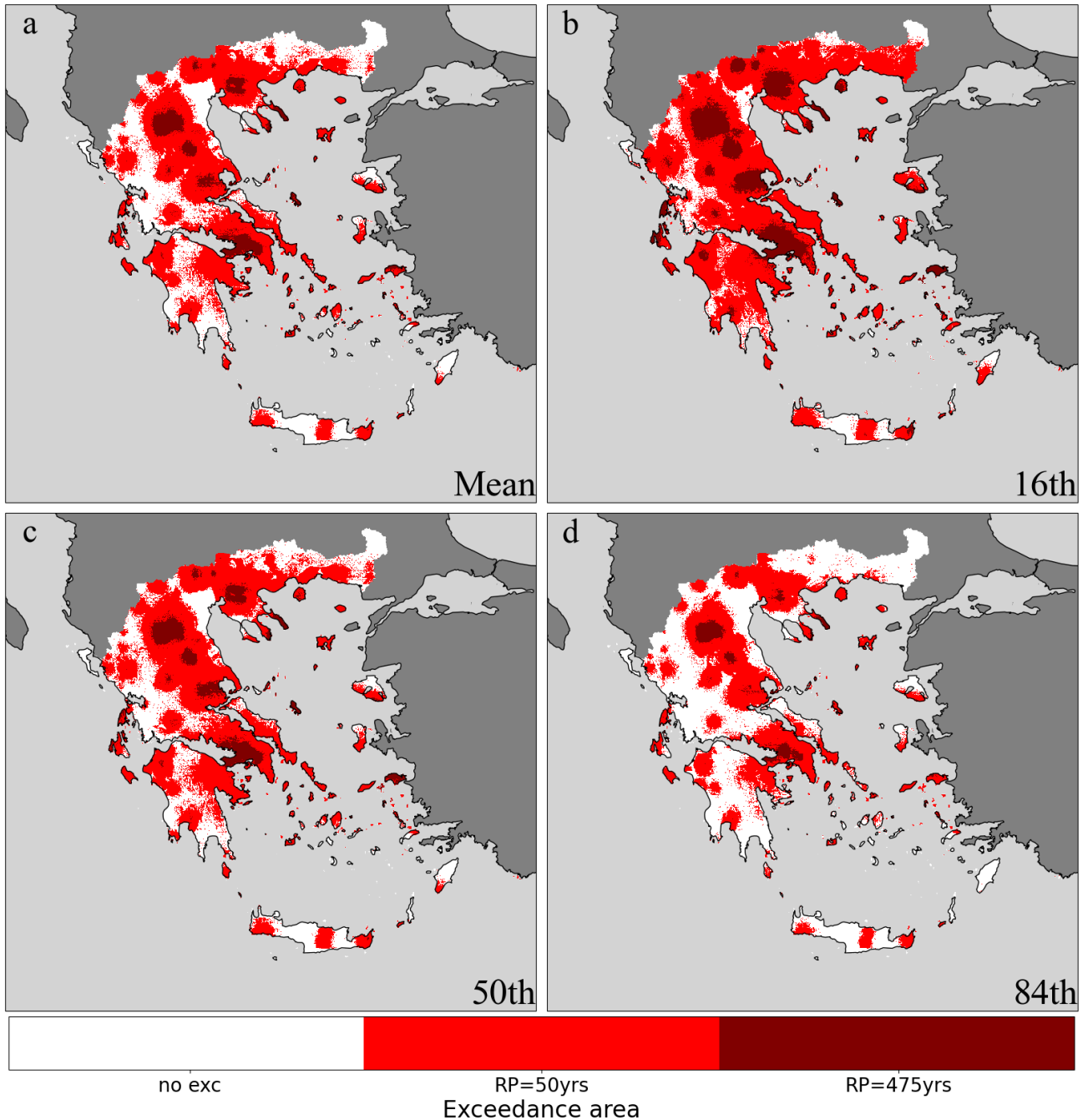


Figure S4. Fractional exceedance areas where at least one ShakeMap-derived RotD50 spectral acceleration at $T = 0.3$ s ($Sa[0.3$ s]) exceeded the corresponding ESHM20 hazard thresholds. The $Sa(0.3$ s) intensity measure is relevant for mid-rise building typologies commonly found in Greece, with fundamental periods on the order of 0.3–0.4 s. Colour shading, consistent with Figure 5, indicates the presence of exceedances for the 50-year and 475-year return-period hazard levels. Spatial variability reflects the combined effects of ground-motion model variability within the ShakeMap logic tree and site-response adjustments, rather than systematic bias in the ESHM20 hazard model.

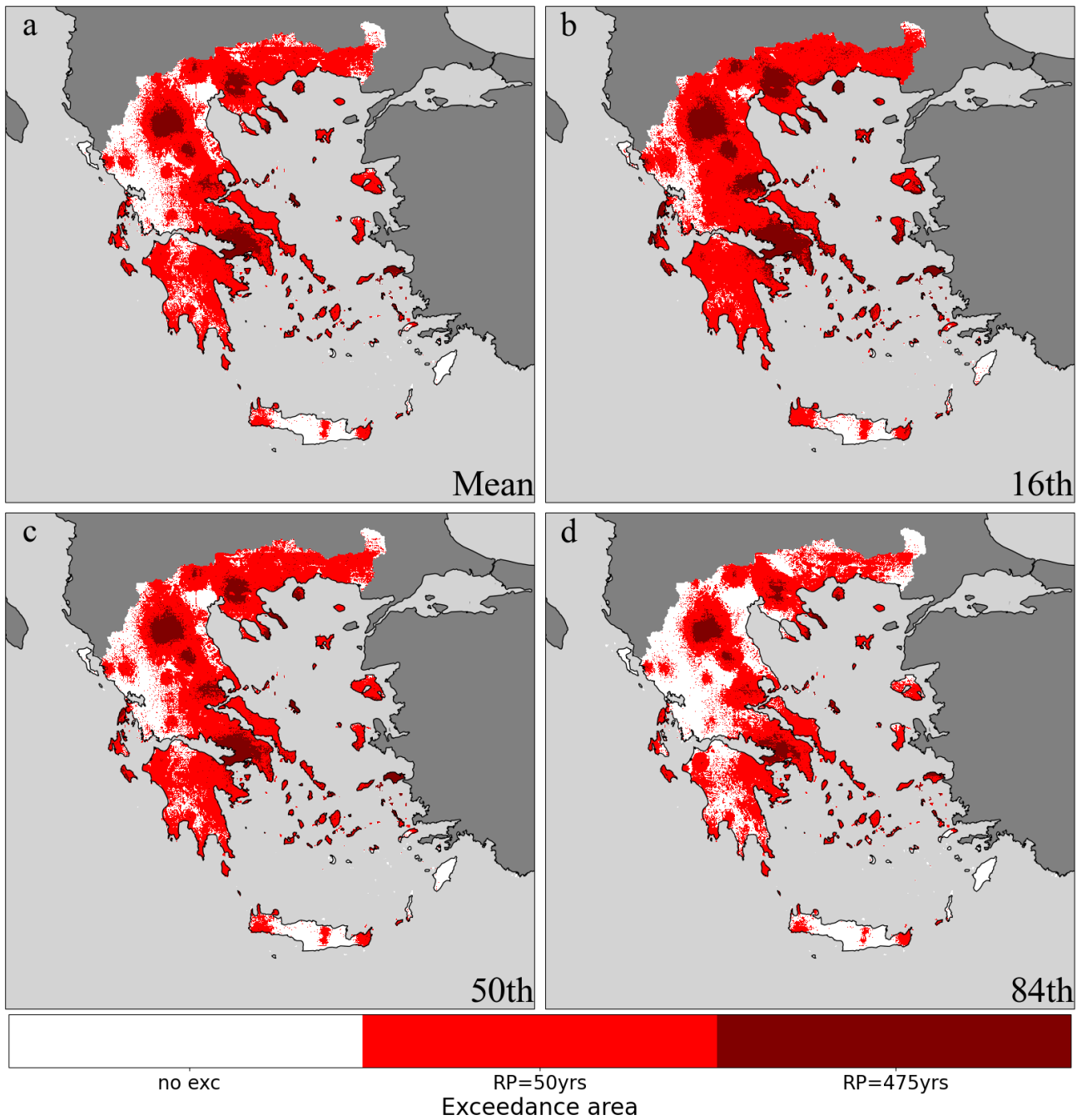


Figure S5. As in Fig. S4 for spectral acceleration at $T=1.0$ second ($S_a[1.0s]$).

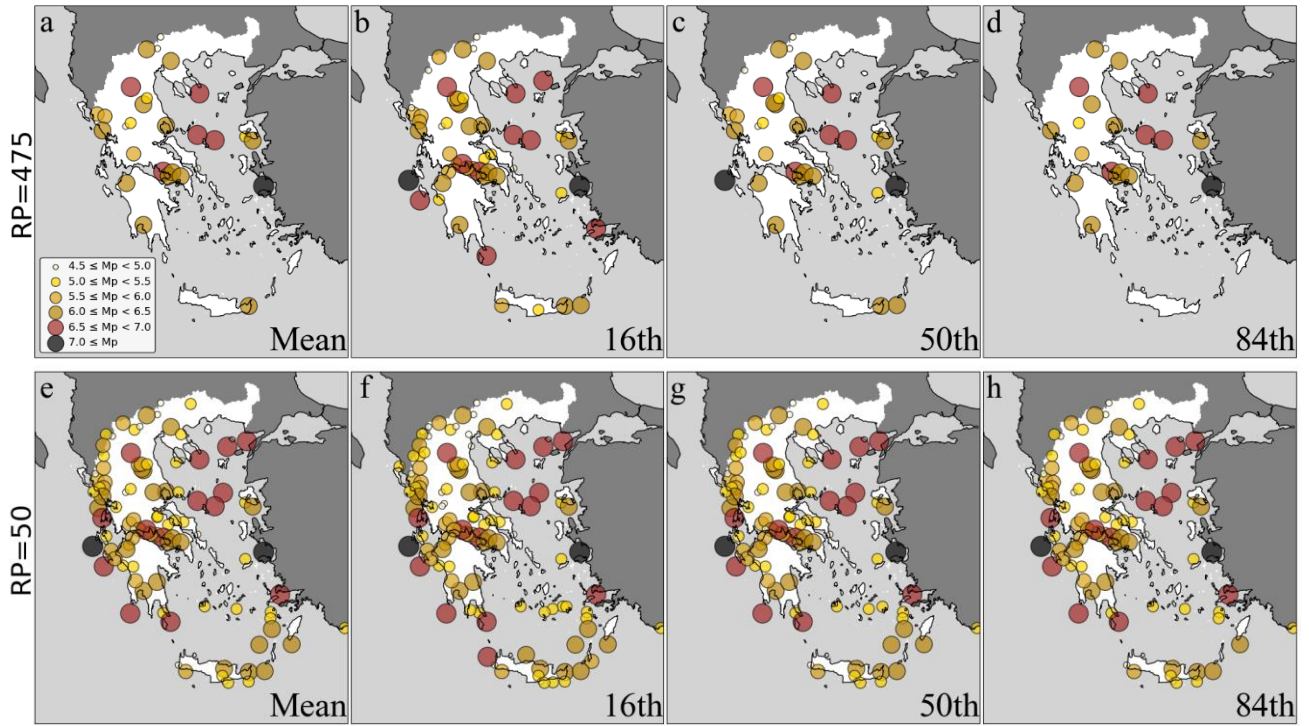


Figure S6. Spatial distribution of earthquake epicentres (circles, coloured by potency magnitude, M_p) associated with at least one exceedance of the ESHM20 RotD50 spectral acceleration hazard thresholds at $T = 0.3$ s ($S_a[0.3$ s]) in the ShakeMap-derived ground-motion fields. Panels (a–d) correspond to exceedances relative to the 475-year return-period hazard levels, and panels (e–h) to the 50-year return-period hazard levels. Columns show different aggregation levels of the ESHM20 hazard model: mean, 16th percentile, 50th percentile (median), and 84th percentile.

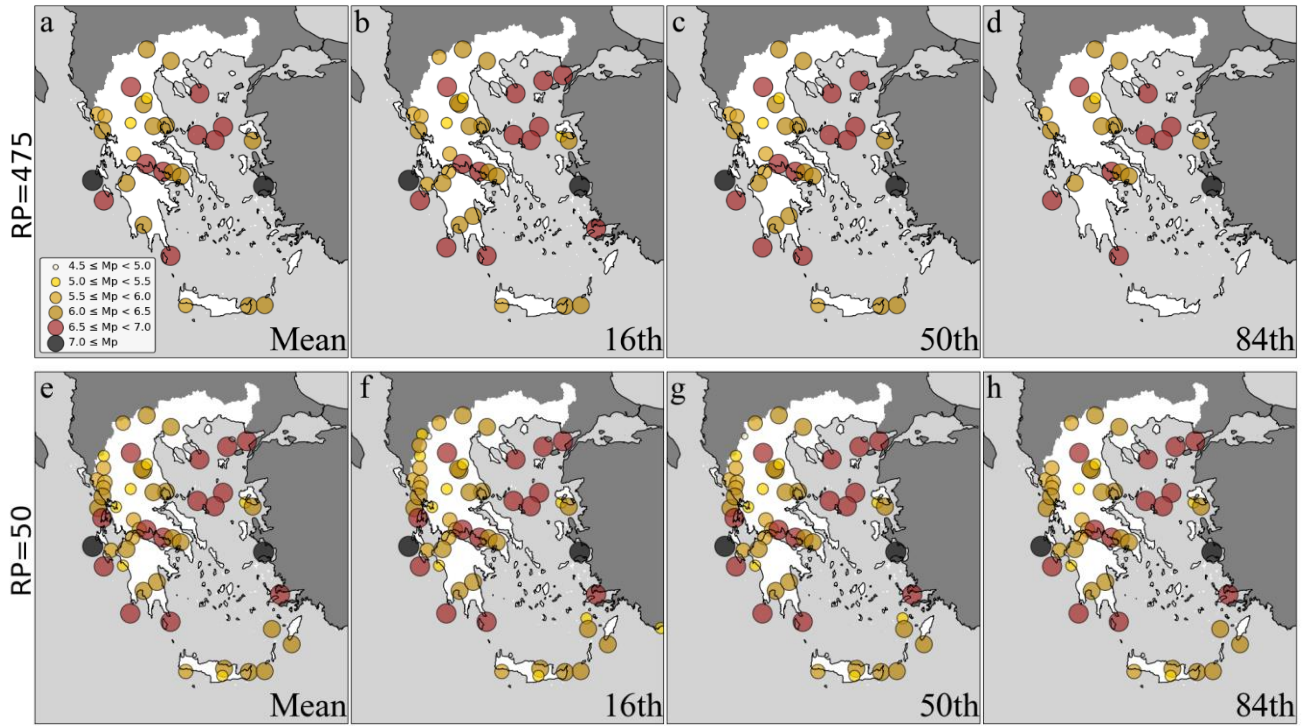


Figure S7. As in Figure S6, but for RotD50 spectral acceleration at $T = 1.0$ s ($Sa[1.0$ s]). Spatial distribution of earthquake epicentres (circles, coloured by potency magnitude, M_p) associated with at least one exceedance of the ESHM20 hazard thresholds in the ShakeMap-derived ground-motion fields, shown for return periods of 475 years (a–d) and 50 years (e–h), and for different aggregation levels of the ESHM20 hazard model (mean, 16th, 50th, and 84th percentiles).

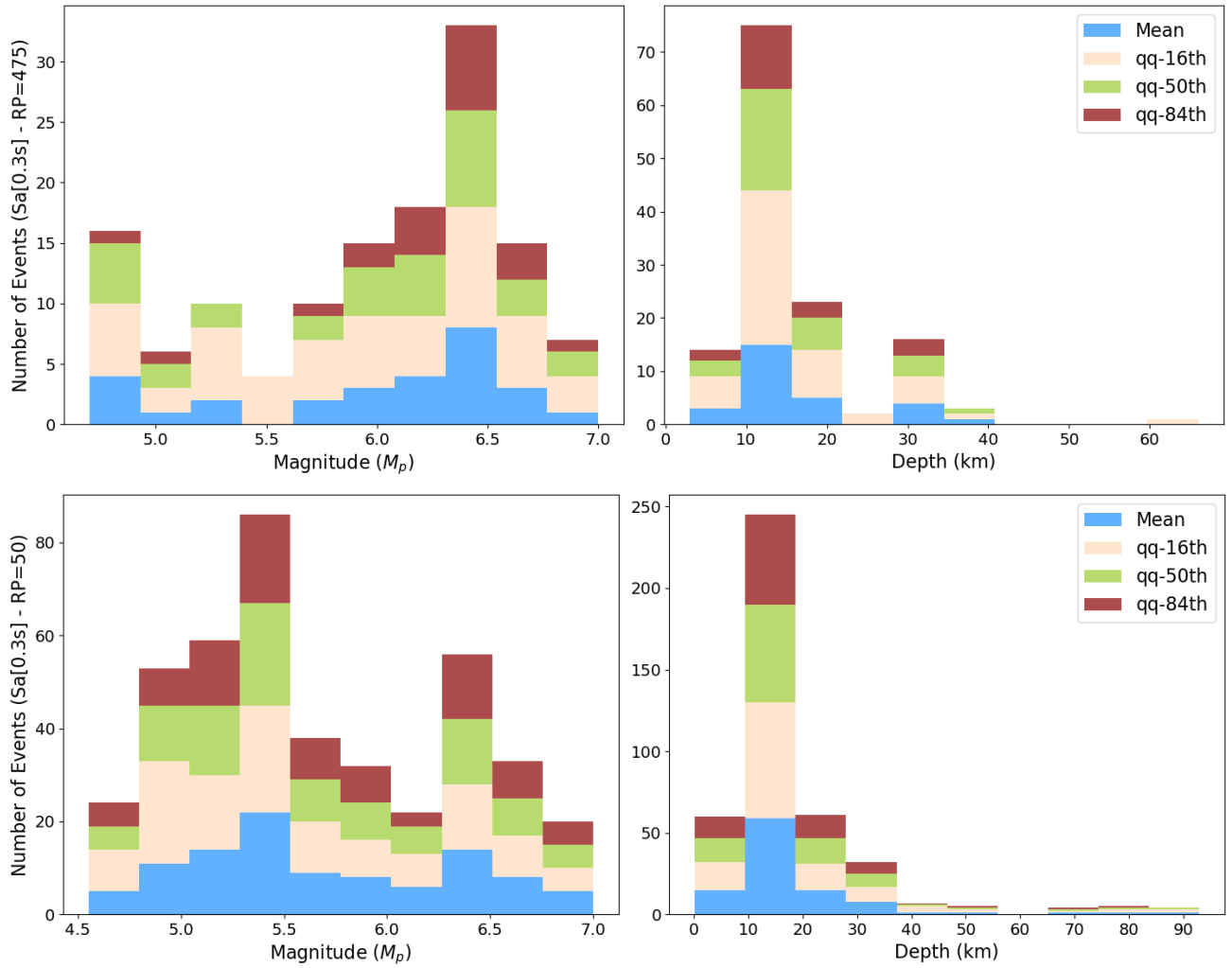


Figure S8. Number of earthquake events associated with at least one exceedance of the ESHM20 RotD50 spectral acceleration hazard thresholds at $T = 0.3$ s ($Sa[0.3$ s]) in the ShakeMap-derived ground-motion fields, shown as a function of potency magnitude and focal depth. The top row corresponds to exceedances relative to the 475-year return-period hazard levels, and the bottom row to the 50-year return-period hazard levels. Coloured bars indicate exceedance counts for different aggregation levels of the ESHM20 hazard model (mean, 16th percentile, 50th percentile, and 84th percentile).

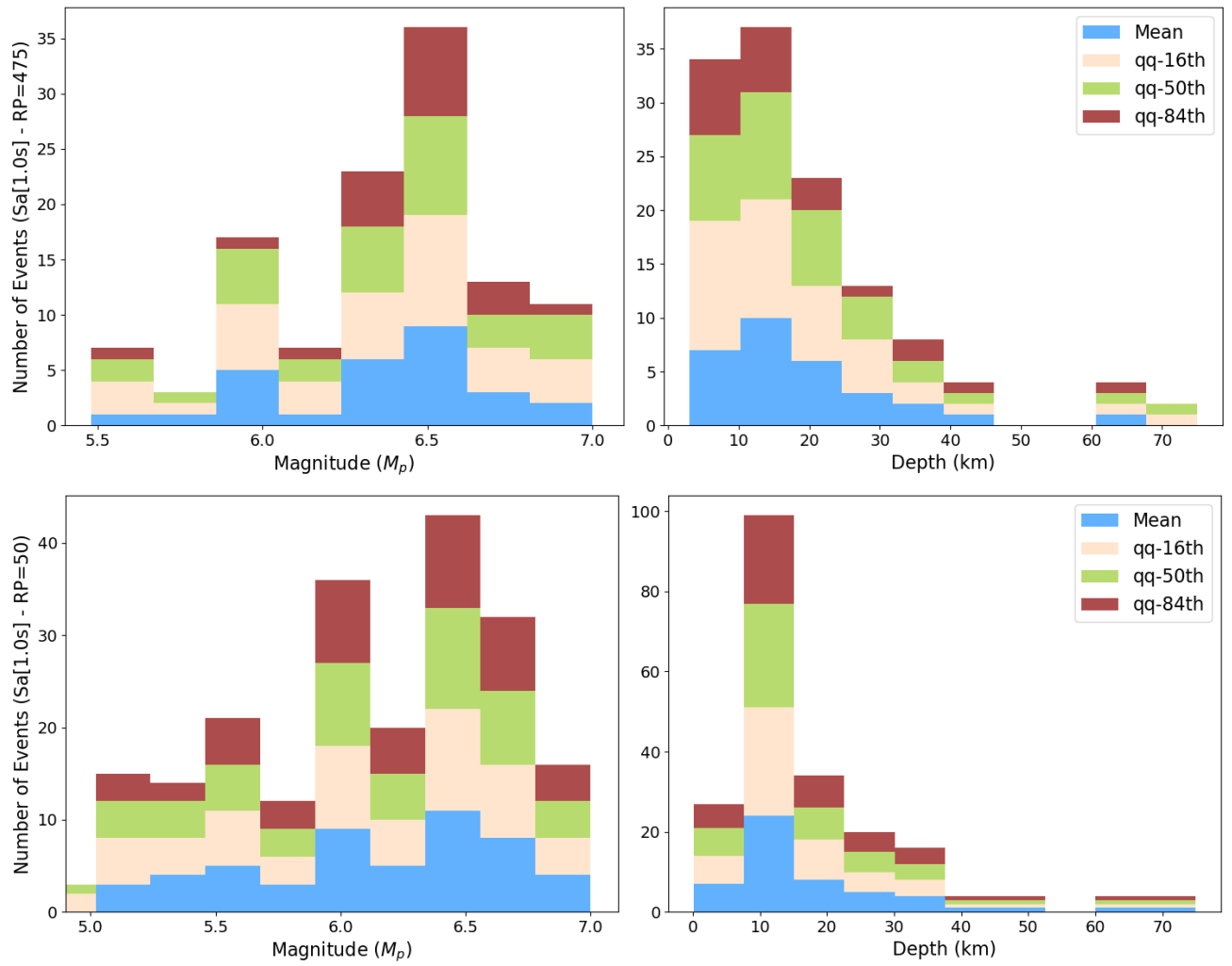


Figure S9. As in Fig. S8, but for RotD50 spectral acceleration at $T = 1.0$ s ($Sa[1.0$ s]).

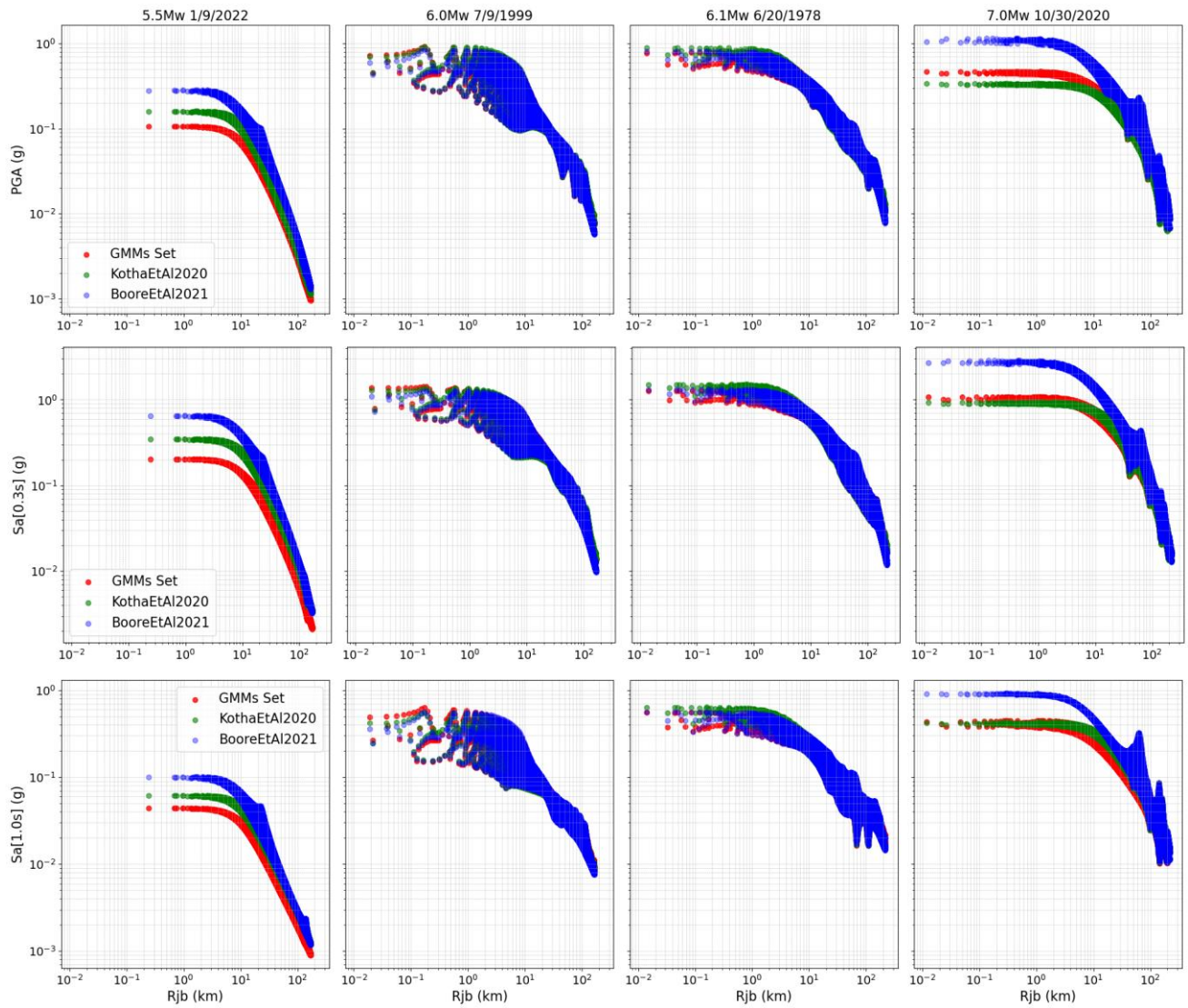


Figure S10. Distance–attenuation behaviour of ShakeMap-derived intensity measures (IMs) as a function of Joyner–Boore distance (R_{jb}) for four representative earthquakes in Greece: (a) Mw 5.5, 1 September 2022; (b) Mw 6.0, 7 September 1999 (Athens); (c) Mw 6.5, 20 June 1978 (Thessaloniki); and (d) Mw 7.0, 30 October 2020 (Samos). Rows correspond to different intensity measures: peak ground acceleration (PGA, top row), spectral acceleration at $T = 0.3$ s ($Sa[0.3\text{ s}]$, middle row), and spectral acceleration at $T = 1.0$ s ($Sa[1.0\text{ s}]$, bottom row). For each event and intensity measure, ShakeMaps were generated using three alternative ground-motion modelling configurations: a composite model combining four active-crustal GMMs used in the ShakeMap logic tree (red; see Table 1), the Kotha et al. (2020) GMM (green), and the Boore et al. (2021) GMM (blue). The figure illustrates the range of model-dependent attenuation behaviour that contributes to epistemic variability in ShakeMap ground-motion fields.

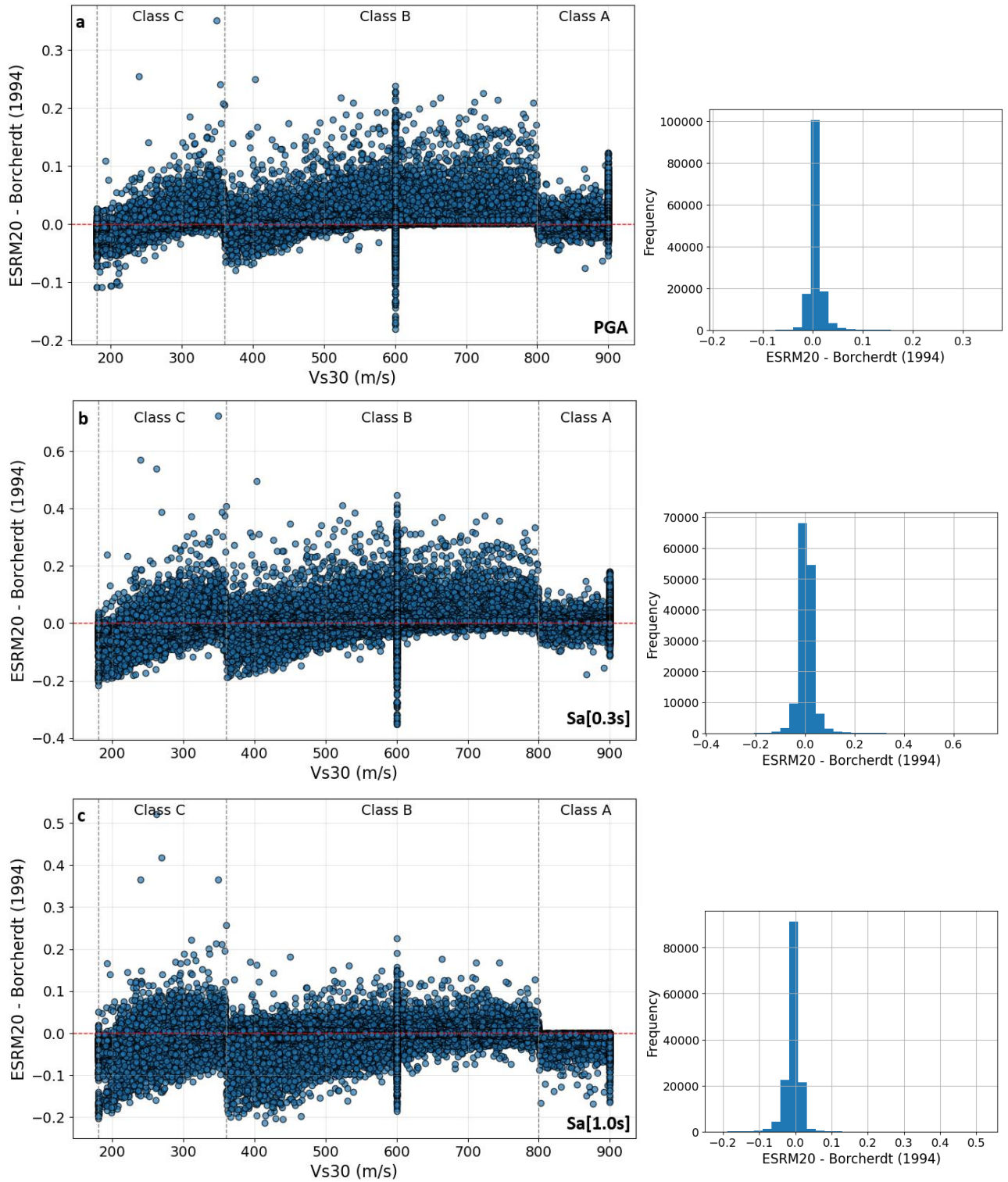


Figure S11. Differences in intensity measures (IMs) obtained using rock-site amplification factors from the European Site Response Model (ESRM20; Weatherill et al., 2021) relative to those derived from the Borchardt (1994) formulation, shown as a function of V_{s30} . Positive values indicate larger IM values after adjustment with ESRM20 compared to Borchardt (1994). Vertical dashed lines denote Eurocode 8 site-class boundaries (Classes C, B, and A). Right-hand panels show the corresponding frequency distributions of the IM differences. Panels correspond to (a) peak ground acceleration (PGA), (b) spectral acceleration at $T = 0.3$ s ($S_a[0.3\text{ s}]$), and (c) spectral acceleration at $T = 1.0$ s ($S_a[1.0\text{ s}]$). The scatter highlights increased variability near site-class boundaries, illustrating how differences in site-response parameterisation can contribute to residual variability in ShakeMap-derived ground-motion fields.

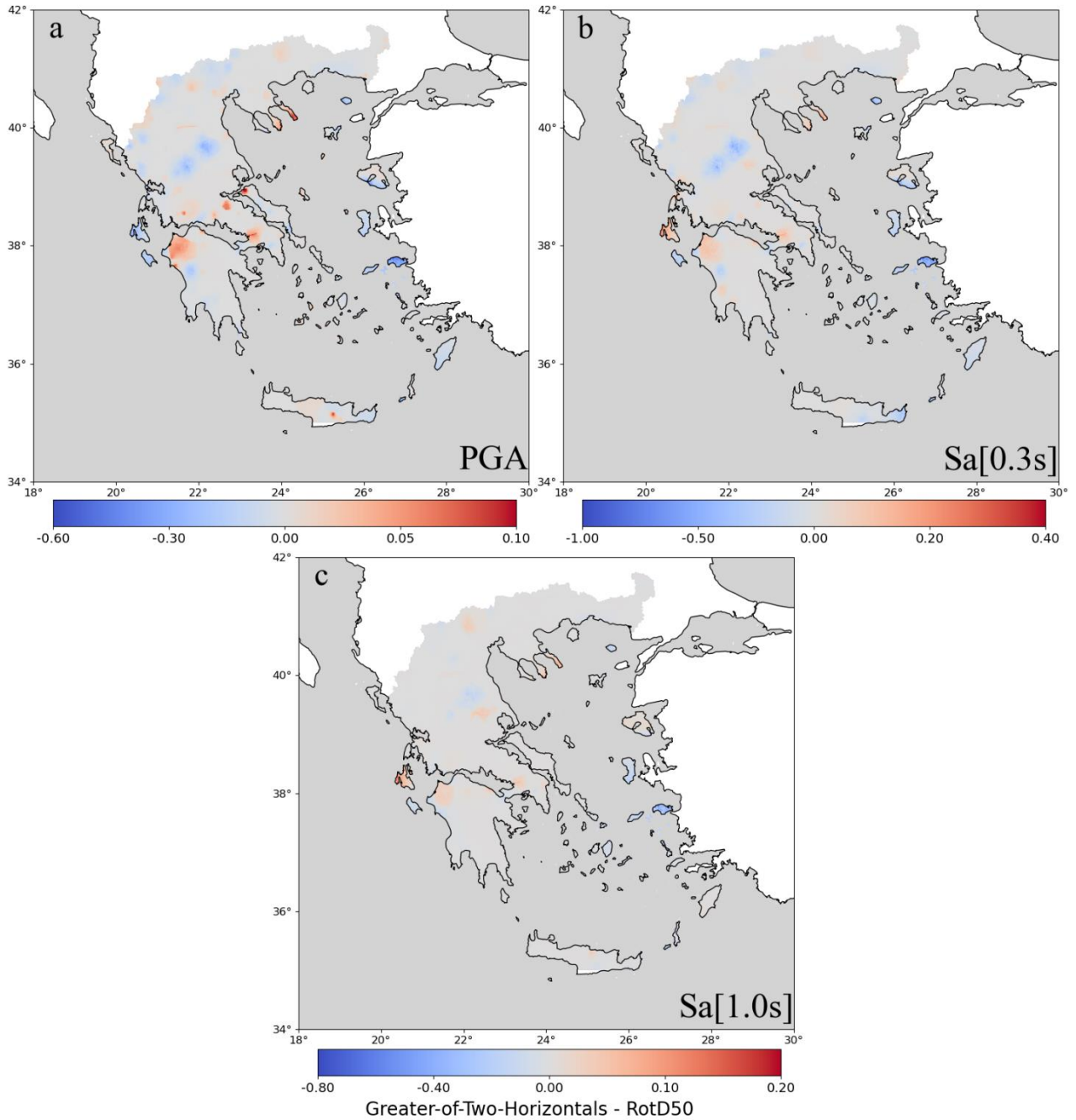


Figure S12. Spatial distribution of the difference between intensity measures (IMs) computed using the greater-of-two-horizontal components and the rotation-independent RotD50 definition. Positive values (red) indicate locations where the greater-of-two-horizontals approach yields larger IM values than RotD50 (Boore, 2010). Panels show results for (a) peak ground acceleration (PGA), (b) spectral acceleration at $T = 0.3$ s ($Sa[0.3s]$), and (c) spectral acceleration at $T = 1.0$ s ($Sa[1.0s]$). Differences reflect component-definition effects rather than physical changes in ground shaking and illustrate the magnitude and spatial variability of IM conversion effects relevant for comparison with ESHM20 hazard maps.